International Journal of Multiphysics
Volume 18, No. 2s, 2024
ISSN: 1750-9548

A Multilevel Investigation into Tip Wake of Wind Turbine Using Sirovich-type Proper Orthogonal Decomposition

Weimin Wu[1, 2], Xiongfei Liu[3,*], Jianyao Yao[4], Zhongjun He[5], Wenqiang Du[3], Suocheng Zhang[6], Liang Li[1]

[1]. School of Mechanical and Power Engineering, Chongqing University of Science and Technology, Chongqing, 401331, China
[2]. Nanchang Institute of Technology, Nanchang, 330044, China
[3]. Yinchuan University of Science and Technology, Yinchuan, 750001, China
[4]. College of Aerospace Engineering, Chongqing University, Chongqing, 400044, China
[5]. Sichuan Aerospace System Engineering Research Institute, Chengdu, 610100, China
[6]. Inner Mongolia Three Gorges Mengneng Energy Co., Ltd., Hohhot, 010090 China
[*] Corresponding author 2019008@cqust.edu.cn

Abstract
It is still challenging to study the multi-level flow of complex rotating tip wake and give a reasonable physical explanation. Based on the multi-relaxation time lattice Boltzmann method, a high-fidelity numerical model is established to provide a valid and rational data base. At the same time, a methodology is presented to resolve the complex rotating flow wake based on discrete Sirovich-type proper orthogonal decomposition. Moreover, a critical sub-region with a discrete strategy in the methodology is determined to realize data homology and reduce calculation. The results indicate that the 1st-order flow modes have the macroscopic average flow characteristics of the blade tip wake, corresponding to the zero-frequency peak. The 2nd-order and 3rd-order flow modes are the energy mapping of the tip wake, indicating a remarkable circumferential symmetry. As the order increases, the flow modes first projected by the blade tip wake, followed by the flow modes projected by the attached vortex or X-axial velocity, and then the flow modes projected by deep fusion of the tip wake and the attached vortex or X-axial velocity. The deep fusion reflects the quasi-resonance mechanism of the local wake flow structures of the blade tip vortices, which also corresponds to the energy content and time-frequency characteristics respectively.

Keywords: Multilevel rotating flow, Sirovich-DPOD method, flow mode, time coefficient

1 INTRODUCTION

There are still many key issues to be addressed in the aerodynamics of wind turbines, as it is directly related to the generation of power by wind turbines [1]. Due to a series of aerodynamic problems, it is difficult to accurately predict the aerodynamic load level and its distribution characteristics and power coefficients of a horizontal axis wind turbine [2]. This requires a deep understanding of the aerodynamic characteristics of wind turbines and the development characteristics of wake to improve design.

There are two experimental measurement methods, wind tunnel and external field, which can provide effective verification for the analysis of theoretical models and numerical models. They include the Particle Image Velocimetry (PIV) [3], power coefficient of model wind turbines, power system stability [4], velocity distribution and velocity recovery characteristics of wind turbine flow field under different turbulence intensities, and speed recovery characteristics [5-7]. Through wind tunnel experiments, some scholars have studied the characteristics of the wake field of a horizontal-axis wind turbine in the atmospheric boundary layer [8], and

other aerodynamic performance [9], as well as the influence of wake vortex structure and wind turbine structure dynamics [10].

However, experimental measurements are time-consuming, expensive and inflexible for different operation conditions. They require high-precision large-scale numerical calculation methods, such as computational flow dynamics, to analyze the aerodynamic load and wake characteristics of wind turbines to supplement the deficiencies of experiments.

In numerical calculation [11-12], the methods for wind turbine aerodynamics generally include the blade element momentum method (BEM), the free vortex wake method (FVW), and the computational fluid dynamics method (CFD). Compared with the other two calculation methods, the CFD method can more specifically obtain the flow around the wind turbine blades and the impeller wake in the flow field. It can also predict the dynamic tip vortex evolution [13], three-dimensional effect [14], unsteady incoming flow [15], and dynamic stall [16], as well as the axial force and torque of the entire structure of the impeller [16].

However, the traditional CFD method can only solve the aerodynamic characteristics of the numerical discrete space of the wind turbine wake from a single comprehensive time advancement dimension. It lacks the ability for multi-dimensional spatio-temporal analysis of the complex rotating wake flow field of the impeller, especially for the tip vortex flow structure. This may limit the full understanding of correlation characteristics of the tip vortex flows and analysis of the control effectiveness to some extent. Only considering the blade effects such as the tower and nacelle, De Cillis et al. [17] simulated two cases and analyzed them from the average flow field and POD mode. The results showed that the tip vortices maintained the average shear of the wake, and low-frequency modes contribute to the recovery of the wake. De Cillis et al. [18] also analyzed the modal and non-modal stability of the downstream average flow of the wind turbine rotor, as well as the origin of this coherent structure. The results show that the most energetic structure is caused by modal instability, which triggers a quasi-resonance mechanism in the far wake that determines the occurrence of a specific frequency in turbulence. Hamilton et al. [19] defined a reduced order model (wakeROM) for wind turbine wake using a series of polynomial parameters, which quantified the interaction between modes and the evolution of coefficients for each POD mode. At the same time, the Tikhonov regularization method is used to minimize polynomial parameters and add additional constraints to reduce the coefficient errors of the model, thereby recalibrating the dynamic system. A new initial condition is obtained by a series of open-loop transfer functions that correlated the incoming turbulence velocity to the POD mode coefficient, which periodically reinitializes the wakeROM. However, the above studies are insufficient to analyze the detailed characteristics and laws of the three-dimensional evolution of POD flow modes. In addition, Wood and Hammam [20] analyzed the actuator disc (AD) model of a horizontal axis turbine to determine the optimal performance, defined as the maximum power extracted at any tip speed ratio. The results showed that as the tip ratio increases, the optimal power and thrust asymptotes were close to the familiar Betz-Joukowsky values, and the induced axial velocity and rotor constraint cycle was constant. At low tip velocity ratios, the optimal wake is limited by the need to avoid high vortex rupture, and the traditional thrust equations only involve axial velocity. Versteeg and Malalasekera [21] descripted the finite volume method for computational fluid dynamics. Some deep learning architectures have been also proposed [22-23]. For data-driven large-scale datasets, reference was made to the CFD instantaneous discrete solution dataset limited by fluid dynamic laws, and the invariance of the CFD valid solution datasets deserves further investigation. In our view, the invariance should be closely related to compact and low-dimensional representation in unsupervised learning. In fact, the time-independent wake flow mode of a wind turbine based on proper orthogonal decomposition (POD) [24] should be a typical representative of invariance of a basic dataset.

It is worth studying that the critical high-order flow characteristics and important detailed flow essential information contained in the wake flow field of the wind turbine blade tip vortex. The following structure is organized as: Section 2 briefly describes the Sirovich-DPOD method; Section 3 shows the impeller solid model of the horizontal axis wind turbine and the CFD computation model; Section 4 proposes a methodology based on the Sirovich-DPOD algorithm to resolve the multilevel complicated rotational flow wake of the wind impeller; Section 5 provides the results for the multilevel rotational wake flow patterns, such as a series of

orthogonal wake morphology in a 3D space, a series of energy information, and spectral characteristics of relevant time coefficients. Finally, the findings are drawn.

2 SIROVICH-DPOD METHOD

The POD method can be divided into continuous POD (CPOD) method and discrete POD (DPOD) method. Sirovich [25] improved the original singular value decomposition (SVD) and proposed a more efficient POD-Sirovich process. In this study, a series of in-depth studies on the wake flow field of a rotating wind turbine will be carried out in a 3D physical space using the POD-Sirovich process. The basic data sequence of the Sirovich-DPOD method can be obtained by experimental measurements or based on effective numerical calculations. To understand the Sirovich-DPOD method, it is necessary to clarify two computational concepts: sample vector (SV) and sample matrix (SM). The corresponding matrix expression of SV is as follows:

$$f\left(\mathbf{x},t_j\right)=\left[f\left(x_1,t_j\right)\quad f\left(x_2,t_j\right)\quad\cdots\quad f\left(x_i,t_j\right)\quad\cdots\quad f\left(x_{N_s},t_j\right)\right]^T \tag{1}$$

where x_i is the number of spatially discrete nodes in the study domain; N_s is the overall number of discrete nodes, and t_j is the instantaneous time point of sampling, i.e. snapshot time point. The SV data will be grouped according to the sampling time order to form the original SM.

$$\mathbf{G}=\left[f\left(\mathbf{x},t_1\right)\quad f\left(\mathbf{x},t_2\right)\quad\cdots\quad f\left(\mathbf{x},t_j\right)\quad\cdots\quad f\left(\mathbf{x},t_{N_t}\right)\right] \tag{2}$$

where t_j represents a snapshot time point in chronological order, and N_t is the total number of snapshots. Consequently, **G** is a matrix containing temporal and spatial information with a dimensionality of $N_s \times N_t$.

According to the mathematical and physical significance of **G**, there is a high probability that the original SM has a complete set of orthonormal basis functions $\mathbf{\Phi}$.

The corresponding mathematical projection relationship is as follows:

$$f\left(\mathbf{x},t_j\right)=\sum_{r=1}^{R}c_r\left(t_j\right)\phi_r\left(\mathbf{x}\right),\quad j\in\left[1,N_t\right] \tag{3}$$

and

$$\mathbf{\Phi}=\left[\phi_1\left(\mathbf{x}\right)\quad\phi_2\left(\mathbf{x}\right)\quad\cdots\quad\phi_r\left(\mathbf{x}\right)\quad\cdots\quad\phi_R\left(\mathbf{x}\right)\right] \tag{4}$$

where ϕ_r is the r-order orthogonal space model of the flow field, which has features independent of the time dimension. $c_r\left(t_j\right)$ is the coefficient at the time point t_j corresponding to the *r*-order orthogonal mode, called time coefficient.

The complete set of $\mathbf{\Phi}$ should satisfy the minimum constraint in the sense of square norm. Thus, the optimal description in the energy meaning of the specified physical field can be achieved as follows:

$$\mathbf{\Phi}\Leftrightarrow arg\ min\left[\frac{1}{N_t}\sum_{j=1}^{N_t}\left|\ f\left(\mathbf{x},t_j\right)-\sum_{r=1}^{R}c_r\left(t_j\right)\phi_r\left(\mathbf{x}\right)\right|^2\right] \tag{5}$$

The above mathematical description is equivalent to

$$\mathbf{\Phi}\Leftrightarrow arg\ max\left[\frac{1}{N_t}\sum_{j=1}^{N_t}\left|\ \left(f\left(\mathbf{x},t_j\right),\mathbf{\Phi}\right)\right|^2\right]\ s.t.\ \left(\mathbf{\Phi},\mathbf{\Phi}\right)=1 \tag{6}$$

where $\left(\cdot,\cdot\right)$ represents the inner product, and this constrained maximization problem can be solved by the Lagrange multiplier method.

The key of Sirovich-DPOD method lies in the construction of corresponding covariance matrix as follows:

$$\mathbf{C}=\mathbf{G}^T\mathbf{G} \tag{7}$$

If the number of discrete points in a space is high, the calculation on the following equation will be greatly reduced. This is because the covariance matrix constructed in Eq. (7) is $N_t \times N_t$. The calculation of the corresponding matrix **C only** depends on the number of discrete snapshots. The Sirovich-DPOD method is thus highly effective for CFD calculation of high spatial discrete orders of magnitudes.

Based on the linear algebra and matrix theory, ϕ_r can be linearly represented using the original $\mathbf{G}$.

$$\phi_r = \sum_{j=1}^{N_t} \zeta_j^{[r]} f\left(\mathbf{x}, t_j\right) \tag{8}$$

According to the Lagrange Multiplier Method [26], the *j*-sequence time coefficient of the *r*-order orthogonal flow mode is the *j*-sequence element of the eigenvector corresponding to the *r*-order eigenvalue of the covariance matrix **C**. The matrix characteristic calculation can be written as follows:

$$\mathbf{C}\mathrm{H}_r = \lambda_r \mathrm{H}_r \tag{9}$$

where λ_r is the *r*-order eigenvalue; H_r is the eigenvector, and its eigenvalues is sorted in descending order.

In Eq. (9), H_r expresses the matrix expansion, and it is also the time coefficient matrix of the flow physical parameters.

$$\mathrm{H}_r = \left[h_r(t_1) \quad h_r(t_2) \quad \cdots \quad h_r(t_j) \quad \cdots \quad h_r(t_{N_t})\right] \tag{10}$$

Hence, the flow field mode of the Sirovich-DPOD method is defined as follows:

$$\phi_r(\mathbf{x}) = \frac{1}{N_t \lambda_r} \sum_{j=1}^{N_t} h_r(t_j) f\left(\mathbf{x}, t_j\right) \tag{11}$$

where $\phi_r(\mathbf{x})$ corresponding to the high magnitude λ_r is the main flow mode of the field.

The influence of different flow modes on flow characteristics can be characterized by two generalized energetic parameters, including the single-order energy contribution (SEC) and the cumulative energy contribution (CEC).It is defined as follows:

$$E_s^{[j]} = \frac{\lambda_j}{\sum_{r=1}^{N_t} \lambda_r} \tag{12}$$

and

$$E_c^{[j]} = \frac{\sum_{i=1}^{j} \lambda_i}{\sum_{r=1}^{N_t} \lambda_r} \tag{13}$$

where $E_s^{[j]}$ is the single-order energy contribution degree, and $E_c^{[j]}$ is the cumulative energy contribution degree.

3 IMPELLER MODEL AND CFD MODEL

3.1 Impeller Solid Model

The basic parameters of the S-series new airfoil impeller are shown in Table 1.

Table 1: Basic parameters of a wind turbine impeller

Parameters	Specific values
Number of blades	3
Blade length	0.7 (m)
Wheel diameter	1.4 (m)
Blade tip chord length	0.04 (m)
Aspect ratio of the span to the average chord length	4.22
Blade tip twist angle	5.8 (deg)
Wind turbine blade airfoil	S series a new airfoil
Rated power	300 (W)
Design wind speed	10 (m/s)
Starting wind speed	3 (m/s)

Due to the special position of the wind turbine blade root, it bears a large alternating bending moment, and its stress-strain response will directly affect the vibration mode of the wind turbine blade, and the overall aerodynamics of the wind turbine.

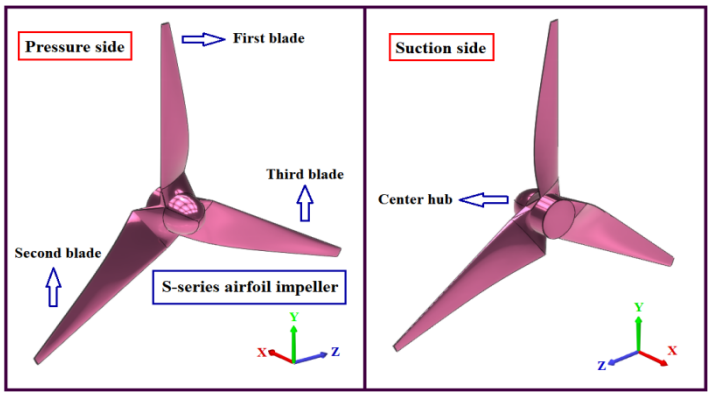

Figure 1: Impeller solid model of the S-series airfoil wind turbine

Considering the dynamics of the wind turbine structure and the problems of blade and hub assembly, some appropriate modifications have been made to the blade root. Figure 1 shows the solid model of the S-series airfoil wind turbine impeller.

3.2 CFD Computation Model

3.2.1 Computation area layout

Before the spatial numerical dispersion of wind turbine tip wake flow field, the calculation area should be effectively divided to ensure that the CFD model has high computational efficiency while obtaining effective accuracy. The specific region division is shown in Figure 2.

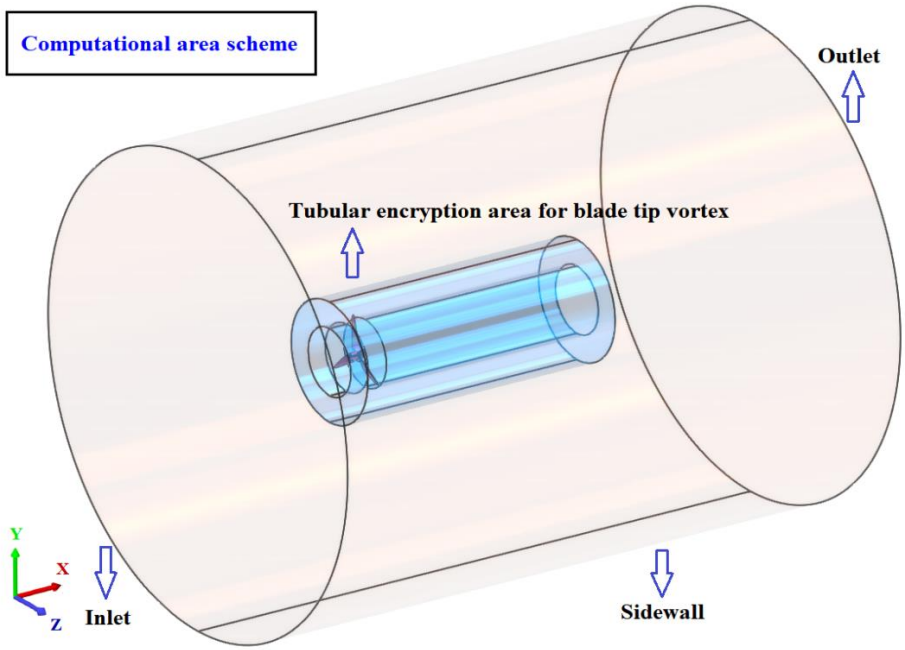

Figure 2: The computational area scheme for the flow field of a tip vortex structure

Taking into account the matching of the geometry of an experimental wind tunnel, and reduction in the influence of the non-physical boundaries of the CFD calculation model, the diameter of the outer calculation area of the cylindrical shape is set to 6 D. D specifies the diameter of the wind impeller. The length of the

cylindrical area along the X-axis is set to 7.5 D. To facilitate the symmetric layout of meshing, the rotation central axis of the impeller and the central axis of the peripheral cylindrical region are set to a coaxial relationship. The intersection point between the scanning surface formed by the rotation of the blade leading edge and the rotation center axis is called the rotation center of the impeller. The X-axial distance between the rotating center of the impeller and the left end face of the outer cylinder is set to 2.13 D.

To better capture the spatio-temporal process of the formation, development and change of the tip wake vortex, a tubular encryption area is used. It has an outer diameter of 1.53 D, an inner diameter of 0.85 D, and a length along the X-axis of 3.36 D. To more effectively capture the variation of the flow field on the surface of the rotating impeller, a short cylindrical encryption area is set. Its diameter is set to 0.85 D, and the length along the X-axis to0.25 D.

3.2.2 Spatial discrete grid division

To capture the flow variation near the impeller surface and the vortex wake of the tip, a numerical calculation model based on the multi-relaxation time lattice Boltzmann method (MRT-LBM) [27-29] is used. Compared with the Bhatnagar-Gross-Krook (BGK) collision model, the MRT-LBM model can more realistically approximate the actual hydrodynamic situation. The evolution of the MRT-LBM model is expressed as follows:

$$\left| f_\alpha\left(\vec{r}_i + \vec{e}_\alpha \delta t, t+\delta t\right)\right\rangle - \left| f_\alpha\left(\vec{r}_i, t\right)\right\rangle = -S\left[\left| f_\alpha\left(\vec{r}_i, t\right)\right\rangle - \left| f_\alpha^{eq}\left(\vec{r}_i, t\right)\right\rangle \right] \tag{14}$$

where f_α indicates the velocity distribution function in the computational domain. It can satisfy the number density distribution of kinetic particles at the position $\vec{r}_i$, and *t* represents the time. e_α is the discrete velocity vector of particles moving in space; f_α^{eq} is the equilibrium distribution function, and ***S*** is the collision matrix operator. The transformation matrix mapping is necessary for actual calculation [29]. The D3Q27 model is used to realize the spatial dispersion, which is the maximum number of discrete velocity vectors in the 3D space. Meanwhile, an octree structure algorithm is used for fusion in the spatial dispersion.

The spatial discrete layout scheme of the computational domain is shown in Figure 3. To improve the capture accuracy of the blade tip wake and the computational efficiency of the overall CFD model, as well as the fine transition layer resolution at different spaces, the global resolution scale is set to 0.05 m, and the grid space discrete distribution is Level 1. There are two critically resolved scales for the wake, including the tubular encryption area and the adjacent rotating area of the impeller surface in Figure 2.To improve the stability of the solution and the accuracy of relevant interpolation in the numerical calculation, the resolution scales of the above two grid refinement areas in the CFD model are both set to 0.0125 m, corresponding to the discrete space Level 3.According to the discrete spatial characteristics of the octree structure, the solution scale of this refinement transition layer region is 0.025 m, shown as Level 2 in Figure 3.

For the initialization phase of the CFD model space, the number of fluid grid element series in the corresponding sub-domain is 4,474,392 in Level 1, 6,81,736 in Level 2, and 6,176,704 in Level 3, respectively. The total number of fluid element is 11,332,832, where the boundary fluid element number of the impeller surface and the outer sidewall boundary is 1,83,288, as shown in Figure 2. In the subsequent calculation, due to the relative rotational motion of the wind impeller, the number of spatial discrete grid elements will change in the sub-domains, but with small variation. Technically, the total number of fluid element in the CFD model is about 11.3 million.

International Journal of Multiphysics
Volume 18, No. 2s, 2024
ISSN: 1750-9548

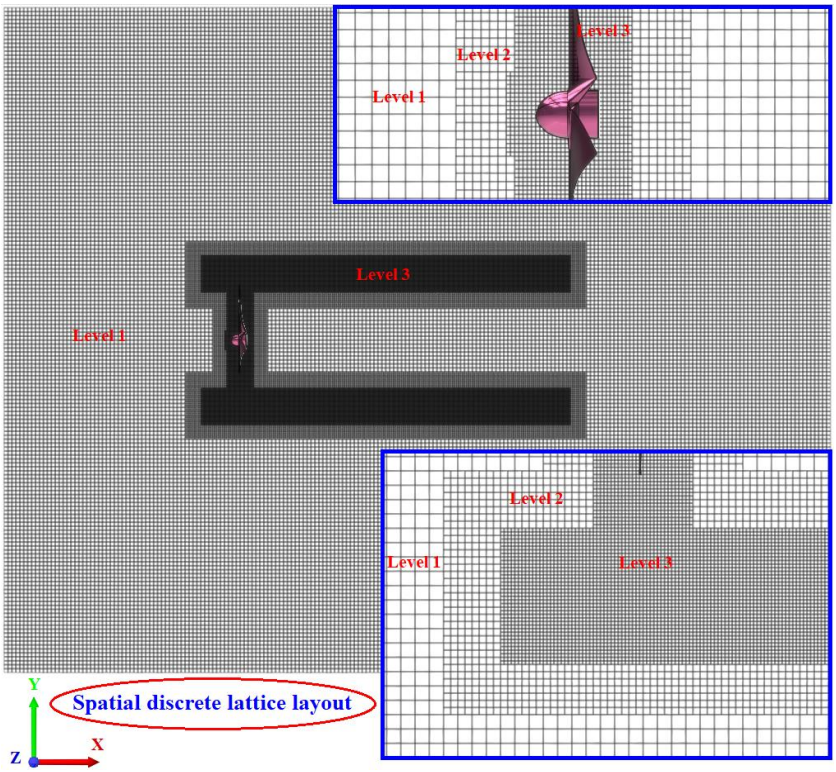

Figure 3: The spatial discrete layout scheme using the octree structure algorithm

3.2.3 Definite solution conditions

Figure 2 is illustrated for reference. In this CFD model, the left end face of the outer cylinder is set as the inlet boundary, which is velocity-inflow type with a wind speed of 10 m/s along the X-axis. The right end face of the outer cylinder is set as the outlet boundary, which is designated as the pressure-outlet type. The initialized absolute static pressure of the flow field is set to 1 standard atmospheric pressure, with a specific value of 101,325 Pa. Based on previous experiments, the initial turbulence intensity is assumed to be 2%. The reference density of the flow medium is 1.225 kg/m^3, and the physically matched dynamic viscosity is approximately 1.7894×10^{-5} Pa.s, which is consistent with the properties of air. Relevant temperature in this domain is set to 288.15 K. A more important parameter is that the wind turbine is designed with a tip speed ratio (TSR) of 5.5, which corresponds to the rotational speed of the impeller of about 750.3 r/min.

To make the calculation more stable and more effective to match the MRT-LBM model, the LBM-LES turbulence model is adopted, where LES refers to large eddy simulation. The key mathematical physics equation is that the integral complete viscosity consists of the fluid molecular viscosity and is the turbulent viscosity [30].

$$\nu = \nu_0 + \nu_t \tag{15}$$

where ν_0 denotes the fluid molecular viscosity coefficient, and ν_t represents the turbulent viscosity coefficient. The variable relaxation time τ is defined as follows:

$$\tau = \frac{\nu}{T} + \frac{\delta t}{2} \tag{16}$$

where T is the temperature in the flow field domain, and δt is the time step in the unsteady computation. Obviously, τ is a variable function, not a deterministic constant used in BGK collision model. For the fluid molecular viscosity coefficient ν_0 in Eq. (15), it is given as follows:

$$\nu_0 = \frac{UL}{Re} \tag{17}$$

where *U* represents the flow velocity feature scale that depends on the physical properties of the fluid molecules. *L* refers to the length feature scale in a flow space, which essentially represents the magnitude of spatial geometry that affects the state of fluid flow.

The turbulent viscosity coefficient ν_t is determined by a series of sub-grid models for LES in small scale turbulent vortex scenarios, mainly because the energy dissipation of small-scale eddies has isotropic characteristics. Here, the wall-adapting local eddy (WALE) viscosity model is selected as the sub-grid turbulence model, which provides a consistent local eddy-viscosity and near-wall behavior for complex aerodynamics [31].

The actual implementation is formulated as follows:

$$\nu_t = \Delta_f^2 \frac{\left(R_{ij}^d R_{ij}^d\right)^{\frac{3}{2}}}{\left(S_{ij}S_{ij}\right)^{\frac{5}{2}} + \left(R_{ij}^d R_{ij}^d\right)^{\frac{5}{4}}} \tag{18}$$

and

$$S_{ij} = \frac{r_{ij} + r_{ji}}{2} \tag{19}$$

and

$$R_{ij}^d = \frac{1}{2}\left(r_{ij}^2 + r_{ji}^2\right) - \frac{1}{3}\delta_{ij} r_{kk}^2 \tag{20}$$

and

$$r_{ij} = \frac{\partial u_i}{\partial x_j} = \sum_{\alpha=1}^{27} e_{\alpha i} e_{\alpha j}\left(f_\alpha - f_\alpha^{eq}\right) \tag{21}$$

where $\Delta_f = C_\omega \Delta x$, Δx is the filter scale of the sub-grid model, and C_ω is the corresponding model coefficient, usually 0.325. In specific calculations, S_{ij} is referred to as the strain rate tensor of the resolved scales, and r_{ij} is defined as the strain rate tensor. r_{ij} is locally available, with the lattice-Boltzmann method as the second-order moment, and extremely efficient in the LES model.

3.2.4 Validity validation of the CFD model

The time-domain history of the aerodynamic parameters of the wind impeller is shown in Figure 4, including the experimental and numerical results. In Figure 4(a), the experimental equivalent measurement results and calculated data of the axial force in the X direction are presented. Due to the influence of experimental measurement errors in equipment and experimental environment, the peak fluctuation of the experimental results is greater than that of the calculated data. However, experimental and computational results indicate that the frequencies of data variation are consistent with the holistic evolution trend. The same data variation characteristics are also reflected in axial torque along the X direction in Figure 4(b).

International Journal of Multiphysics
Volume 18, No. 2s, 2024
ISSN: 1750-9548

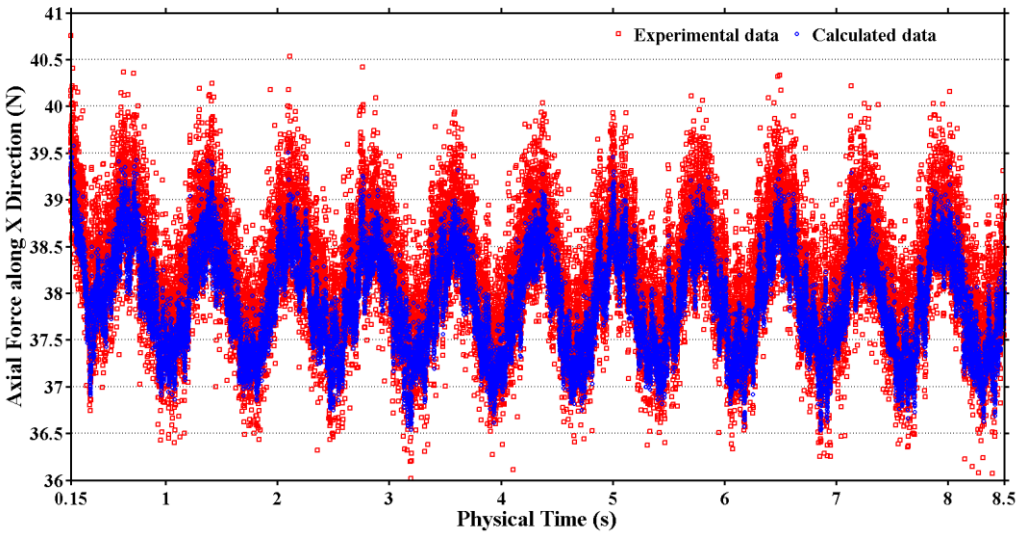

(a) Variation of axial force

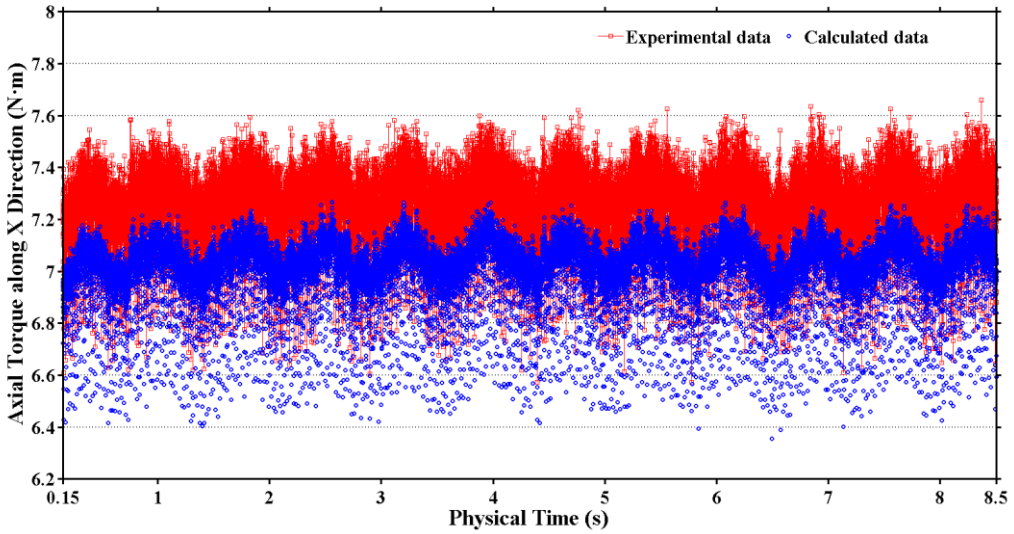

(b) Variation of axial torque

Figure 4: Holistic evolution in time-domain for the aerodynamic parameter results of wind impeller

This indicates that the CFD model based MRT-LBM is reasonable and effective in calculating the complex tip wake flow field of the wind turbine.

4 METHODOLOGY FOR MULTILEVEL INVESTIGATION

The flow characteristics and variation rules of the high-order vortex structure in the tip wake of wind turbines will be deeply quantified and analyzed, so as to provide a reference for the subsequent design of high-efficiency and low-noise wind turbines. The detailed implementation process of the methodology is shown in Figure 5.

International Journal of Multiphysics
Volume 18, No. 2s, 2024
ISSN: 1750-9548

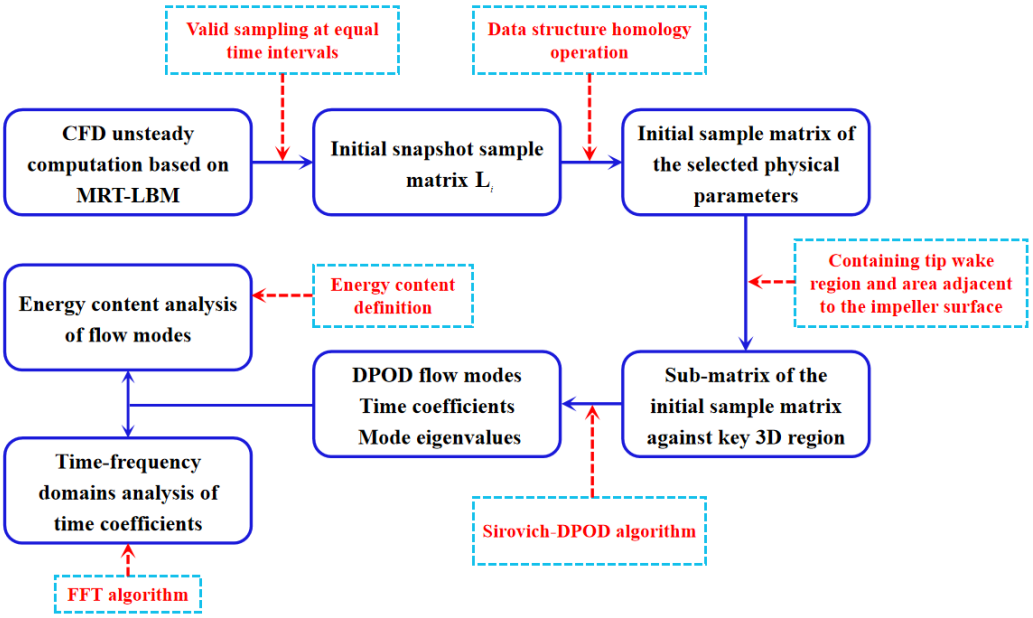

Figure 5: The concrete procedure of DPOD analysis of wind turbine blade tip wake flow field

In addition, the self-developed data interface program used in the DPOD modal analysis of the complex rotational flow of the impeller tip wake is separately explained. The logical and functional architecture is shown in Figure 6.

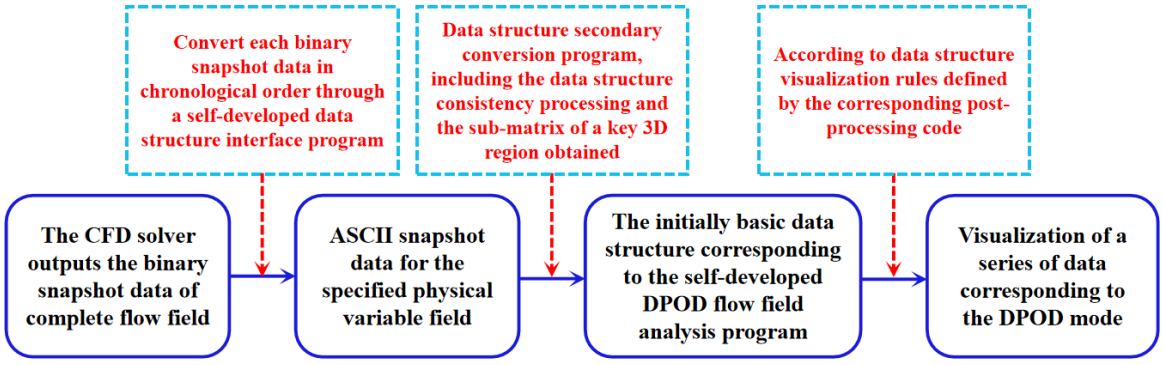

Figure 6: The logical and functional architecture of data structure transformation in DPOD analysis

A self-developed data interface program that studies the wake flow field of DPOD, mainly including three functional roles: converting a series of binary snapshot data into ASCII data types, secondary conversion of ASCII data structures, and visualization of related result data. According to extending the secondary conversion function of the ASCII data structure, this interface program can also be applied to DPOD analysis of other complicated flow problems.

5 ANALYSIS OF RESULTS

To counteract this influence of the discontinuous distribution morphology and improve the level of real physical structure characterization of the DPOD flow modes, the consistent static Cartesian coordinate system is used for each snapshot flow field data. Combined with the orthogonal hexahedral mesh and volume interpolation method, the visual data structure in the identified key 3D sub-region is realized. The selected 3D sub-regions and the spatial discrete grid scheme are shown in Figure 7.

International Journal of Multiphysics
Volume 18, No. 2s, 2024
ISSN: 1750-9548

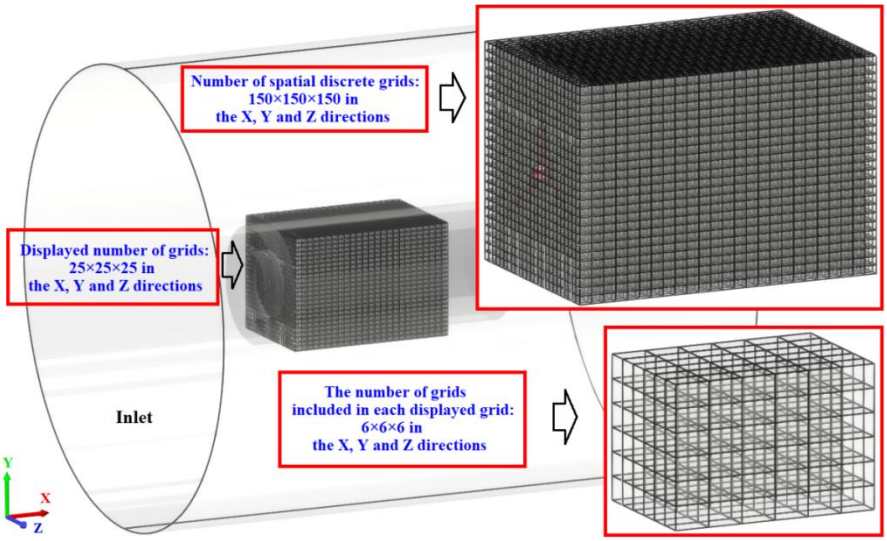

Figure 7: Spatial discrete grid scheme for the 3D sub-region with orthogonal hexahedral mesh

5.1 Spatial Morphology of Flow Modes

The physical parameters of the tip wake flow field include vorticity, velocity modulus and static pressure. DPOD flow modes of the impeller wake flow field will be studied successively according to the above physical parameters.

5.1.1 Vorticity field

The important flow modes of the dimensionless vorticity parameters corresponding to the steady development stage of the wind turbine impeller tip wake are shown in Figure 8.The flow modes from low-to-high order are regular dimensionless, shown as Figures 8(**a**) to (**u**), and the full-order numerical solution at time t = 7.13713 (s) is shown in Figure 8(**v**).

(a)

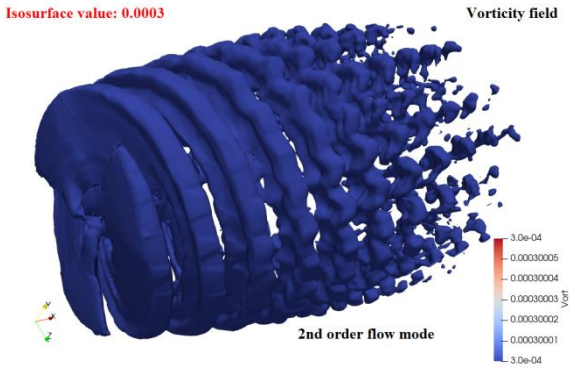

(b)

International Journal of Multiphysics
Volume 18, No. 2s, 2024
ISSN: 1750-9548

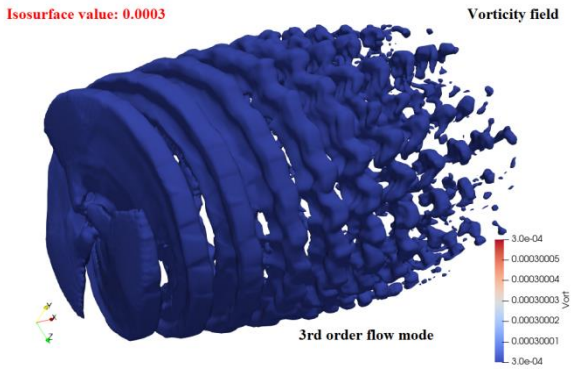

(c)

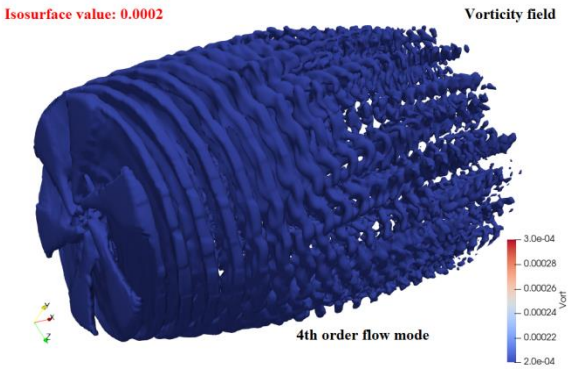

(d)

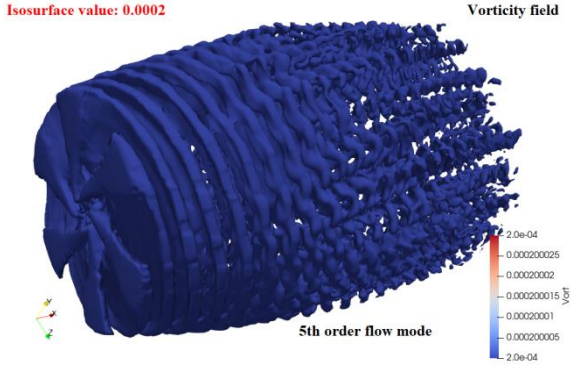

(e)

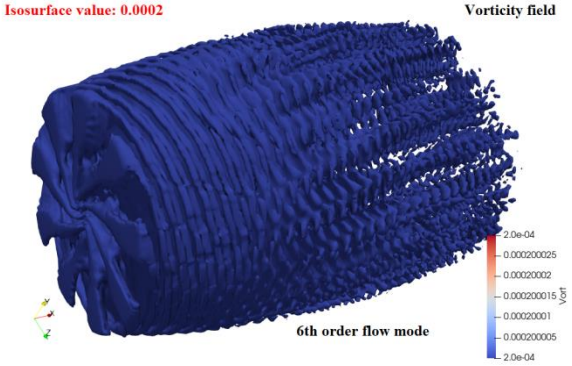

(f)

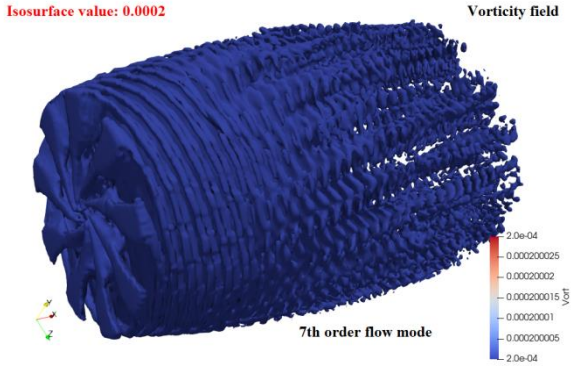

(g)

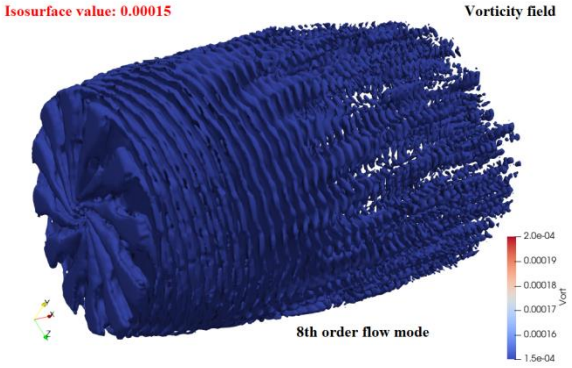

(h)

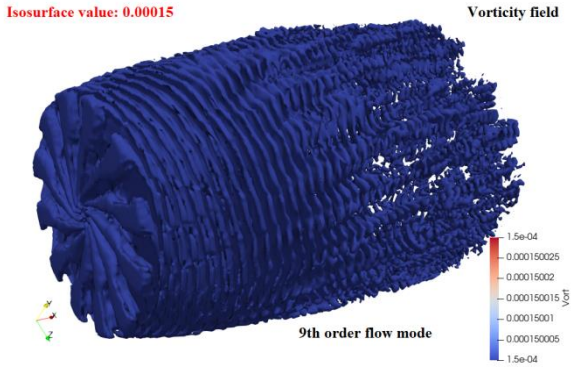

(i)

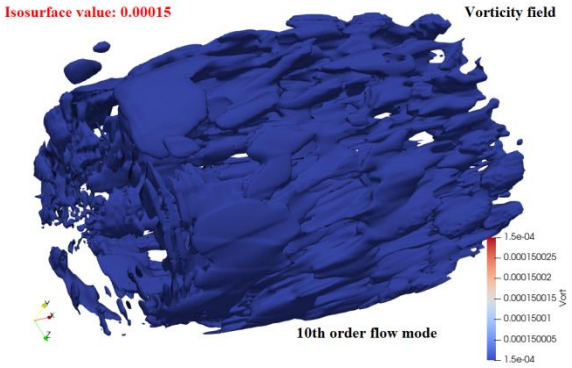

(j)

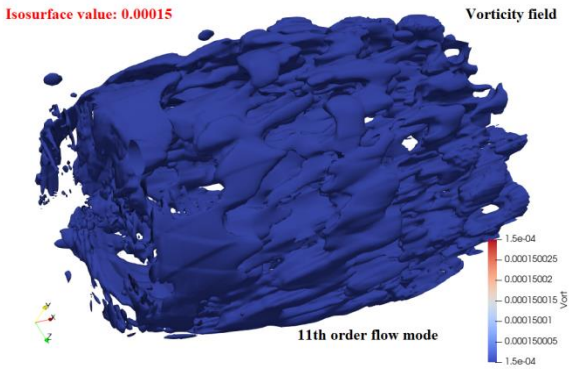
Isosurface value: 0.00015
Vorticity field
11th order flow mode
1.5e-04
0.000150025
0.00015002
0.000150015
0.00015001
0.000150005
1.5e-04
Vort

(k)

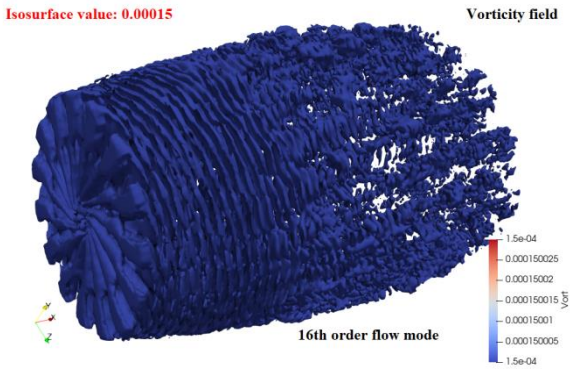
Isosurface value: 0.00015
Vorticity field
16th order flow mode
1.5e-04
0.000150025
0.00015002
0.000150015
0.00015001
0.000150005
1.5e-04
Vort

(l)

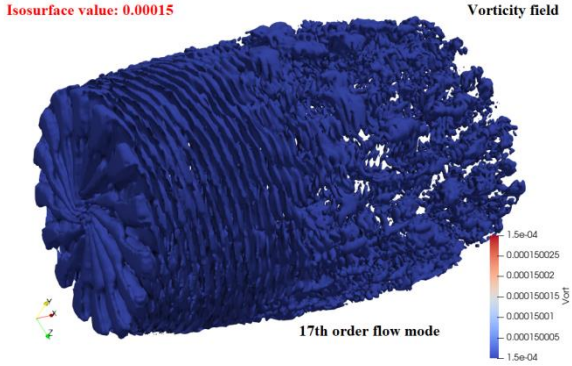
Isosurface value: 0.00015
Vorticity field
17th order flow mode
1.5e-04
0.000150025
0.00015002
0.000150015
0.00015001
0.000150005
1.5e-04
Vort

(m)

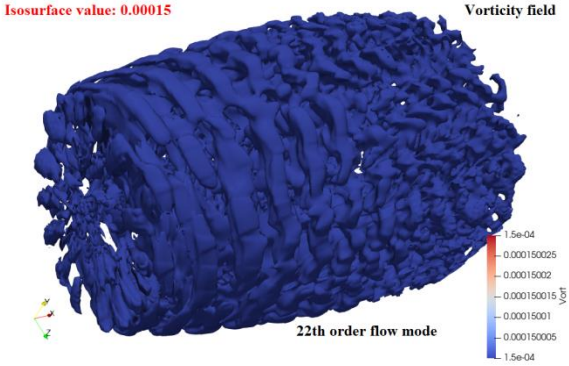
Isosurface value: 0.00015
Vorticity field
22th order flow mode
1.5e-04
0.000150025
0.00015002
0.000150015
0.00015001
0.000150005
1.5e-04
Vort

(n)

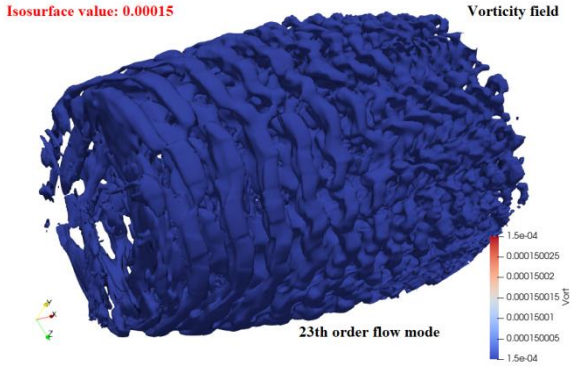
Isosurface value: 0.00015
Vorticity field
23th order flow mode
1.5e-04
0.000150025
0.00015002
0.000150015
0.00015001
0.000150005
1.5e-04
Vort

(o)

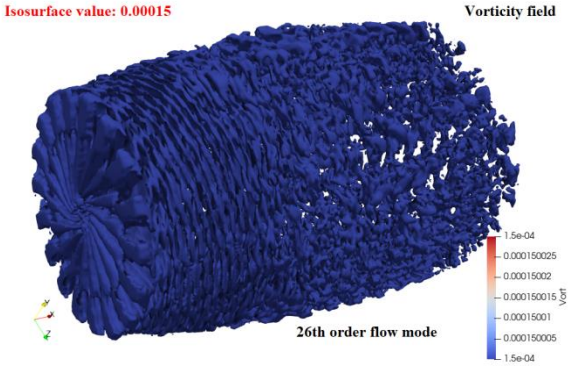
Isosurface value: 0.00015
Vorticity field
26th order flow mode
1.5e-04
0.000150025
0.00015002
0.000150015
0.00015001
0.000150005
1.5e-04
Vort

(p)

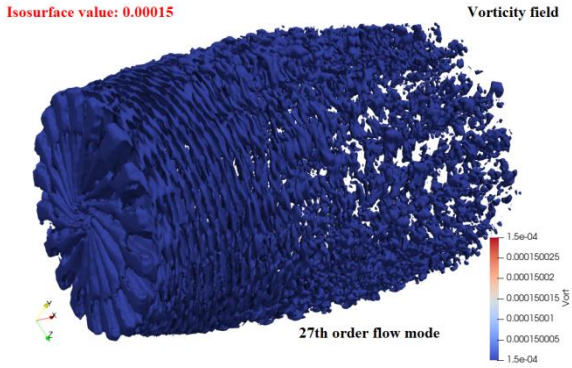
Isosurface value: 0.00015
Vorticity field
27th order flow mode
1.5e-04
0.000150025
0.00015002
0.000150015
0.00015001
0.000150005
1.5e-04
Vort

(q)

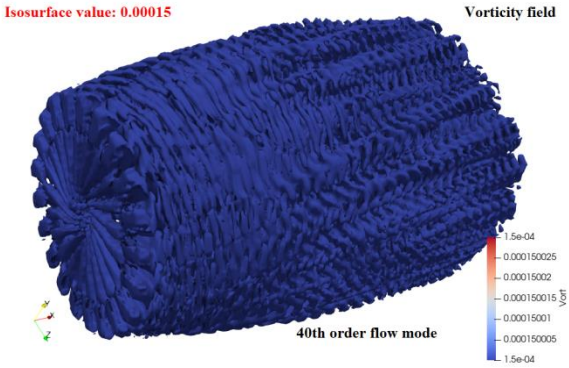
Isosurface value: 0.00015
Vorticity field
40th order flow mode
1.5e-04
0.000150025
0.00015002
0.000150015
0.00015001
0.000150005
1.5e-04
Vort

(r)

International Journal of Multiphysics
Volume 18, No. 2s, 2024
ISSN: 1750-9548

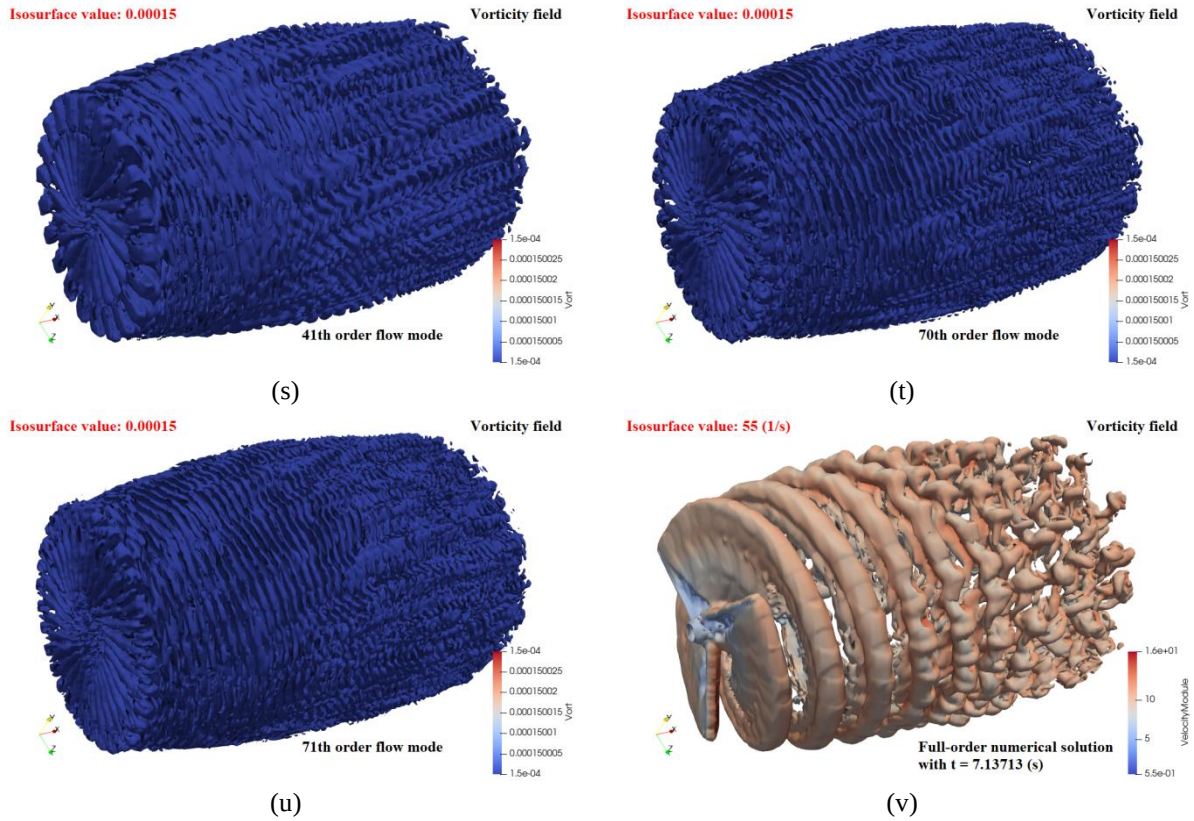

Figure 8: A series of important flow modes of vorticity field and the corresponding full-order numerical solution at a specified transient time point: (a) is the first-order flow mode, representing the macroscopic average flow; (b) - (i), (l) and (m), (p) and (q) are the orderflow modes projected by the blade tip spiral wake; (j) and (k), (n) and (o) are the orderflow modes projected by the blade surface attached vortex wake; (r) to (u) are the orderflow modes projected by the deep fusion of the tip vortex and attached vortex; (v) is the full-order numerical solution of vorticity field at specific transient time points.

To better describe the 3D spatial flow morphology of the blade tip wake vorticity modes, the vorticity isosurface method is adopted. In addition, the values of the isosurface are adjusted according to different mode orders for better representation.

In Figure 8(**a**), it is the first-order flow mode of the tip wake vorticity field, where the isosurface value is set to 0.0005. The region near the swept surface of the impeller is an obvious circumferentially symmetrical disk. As the X axial distance from the rotating surface of the impeller increases, the main influence range of the tip wake along the radial direction of the blade tends to decrease. For macroscopic flow, the 1st-order flow mode represents the overall average flow characteristics of the tip wakes caused by the rotating impeller. The 1st-order flow mode reflects a common average flow physical parameter state, which precisely indicates a significant difference between the average flow state and the subsequent high-order flow mode. Since the average flow mode represents a general macroscopic flow trend and characteristics, the high-order mode reflects the localization and detailed changes of tip vortices in a rotating flow field.

Figures 8(**b**) and (**c**) show the 2nd-3rd order flow modes of the blade tip rotation wake vorticity field, respectively. These two spatial modes are most similar to the transient full-order numerical solution. It is also can be seen that these two flow modes have a conspicuous circumferential symmetry in the 3D space, where the number of local flow structures is consistent with the physical number of blades of the impeller. In addition, the 2nd-3rdsymmetric structures have significant circumferential phase differences. For these two flow modes, the local random fluctuation characteristics of the tip spiral wake is less than that of the full-order numerical solution in Figure 8(**v**). This indicates that the high-order flow modes need to be investigated for further study of the rotating tip wake flow.

Figures 8(**d**) and (**e**) show the 4th-5th order flow modes. Since the energy content of these two modes in the global flow is less than that of the previous ones, the isosurface value is set to 0.0002. As the modal order increases, the number of circumferential symmetric flow structure of the impeller increases to 6, and the phase difference of local symmetric flow structure decreases.

In addition, as the modal order continues to increase, the number of localflow structure increases by a multiple of 3 in Figures 8(**f**) to (**i**). In Figures 8(**j**) to (**k**), they are the 10th and 11th order flow modes, respectively. From the morphological characteristics of their spatial distribution, these spatial flow modes should belong to the wake flow structure of the attached vortices detached from the blade surface. Due to the strong randomness and fluctuation of the formation and shedding of attached vortexes on the surface of each blade, the flow modes are weak in circumferential symmetry, while the random fluctuation characteristics are remarkable.

Figures 8(**l**) and (**m**) show the 16th-17th order wake flow modes, which are the high-order flow modes that project the energy of the tip vortex wake flow. The 22th-23th order flow modes in Figures 8(**n**) and (**o**) show that the wake of the attached vortex on the impeller surface is affected by the spiral wake of the tip vortex. As the mode order increases, the circumferential symmetry of the flow modes projected by the flow energy of the attached vortex wake increases. At the same time, as the mode order increases, these flow modes projected by the attached vortexes of the flow structure are gradually refined compared with those of the 10th and 11th orders.

Figures 8(**p**) and (**q**) show the 26th-27th order flow modes, which belong to the projection of blade tip spiral wakes on the high-order modal space. The characteristics of the random fluctuation of the circumferential distribution is further enhanced.

For high-order flow modes as shown in Figures 8(**r**)-(**u**), the tip vortices and attached vortices further interact, and the spatial modes enter a deep fusion mode. For instance, the 70th-71th order flow modes contain up to 30 circumferential symmetrical structures. The advanced modal space is developing towards further deep integration, with the tip wake structure further refined and the influence of random fluctuations continuously increasing.

5.1.2 Velocity modulus field

Another important flow mode for the dimensionless velocity modulus parameter corresponding to the steady development stage of the impeller wake is shown in Figure 9. Similar to the vorticity field mode, the velocity modulus field mode from low-to-high order is shown in Figures 9(**a**) to (**q**), and the full-order numerical solution at time point of t=7.13713 (s) is shown in Figure 9(**r**). Similarly, the values of the velocity modulus isosurface are adjusted according to different modal orders for better display.

(a)

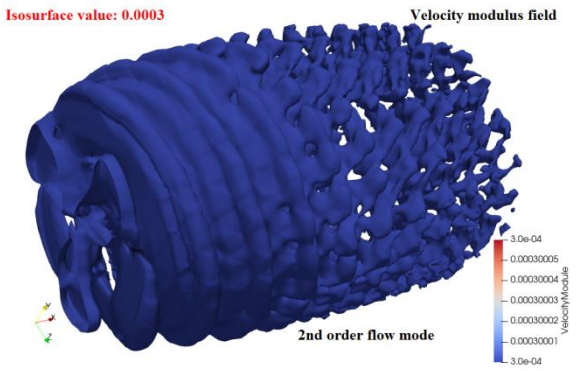

(b)

International Journal of Multiphysics
Volume 18, No. 2s, 2024
ISSN: 1750-9548

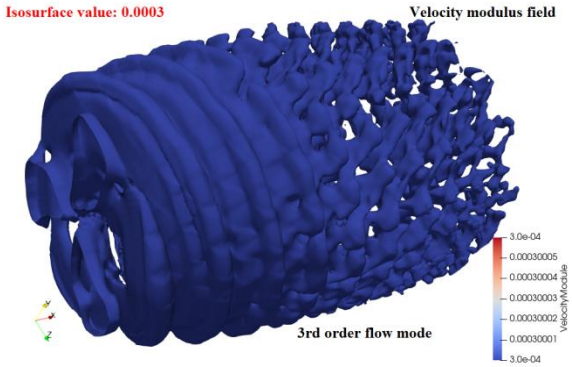

(c)

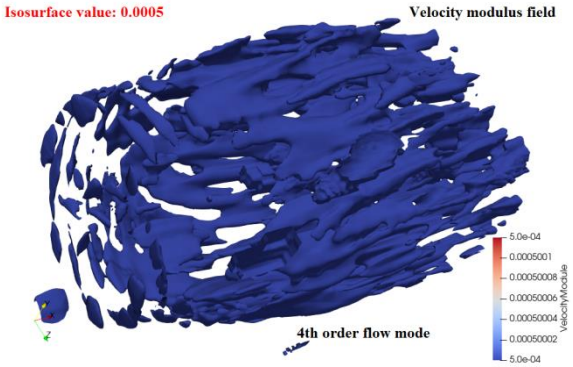

(d)

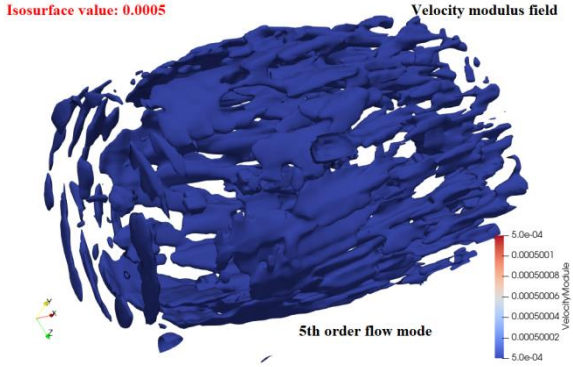

(e)

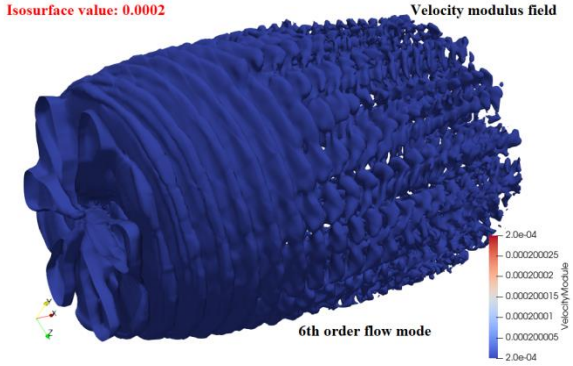

(f)

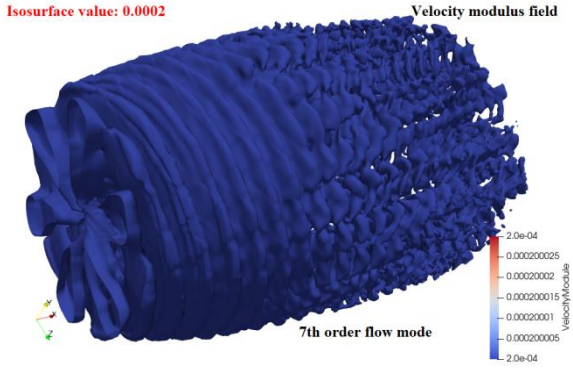

(g)

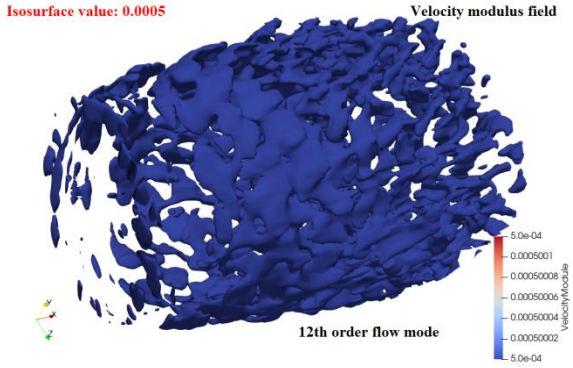

(h)

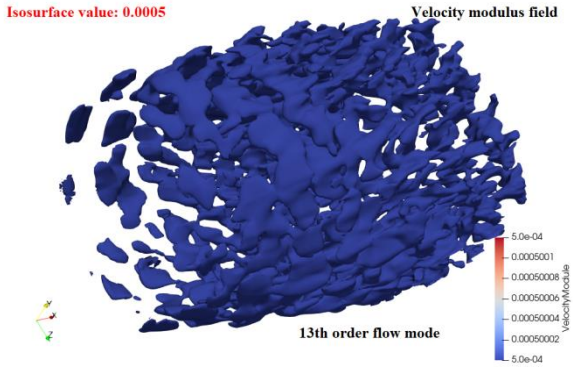

(i)

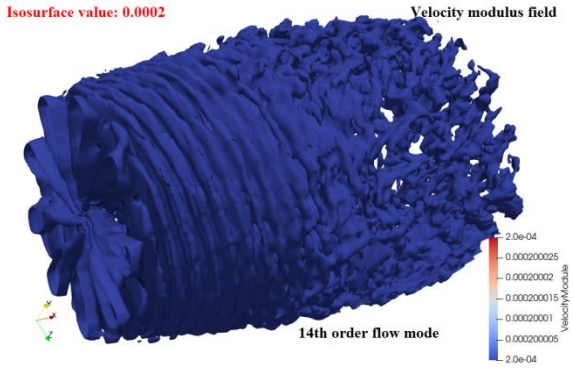

(j)

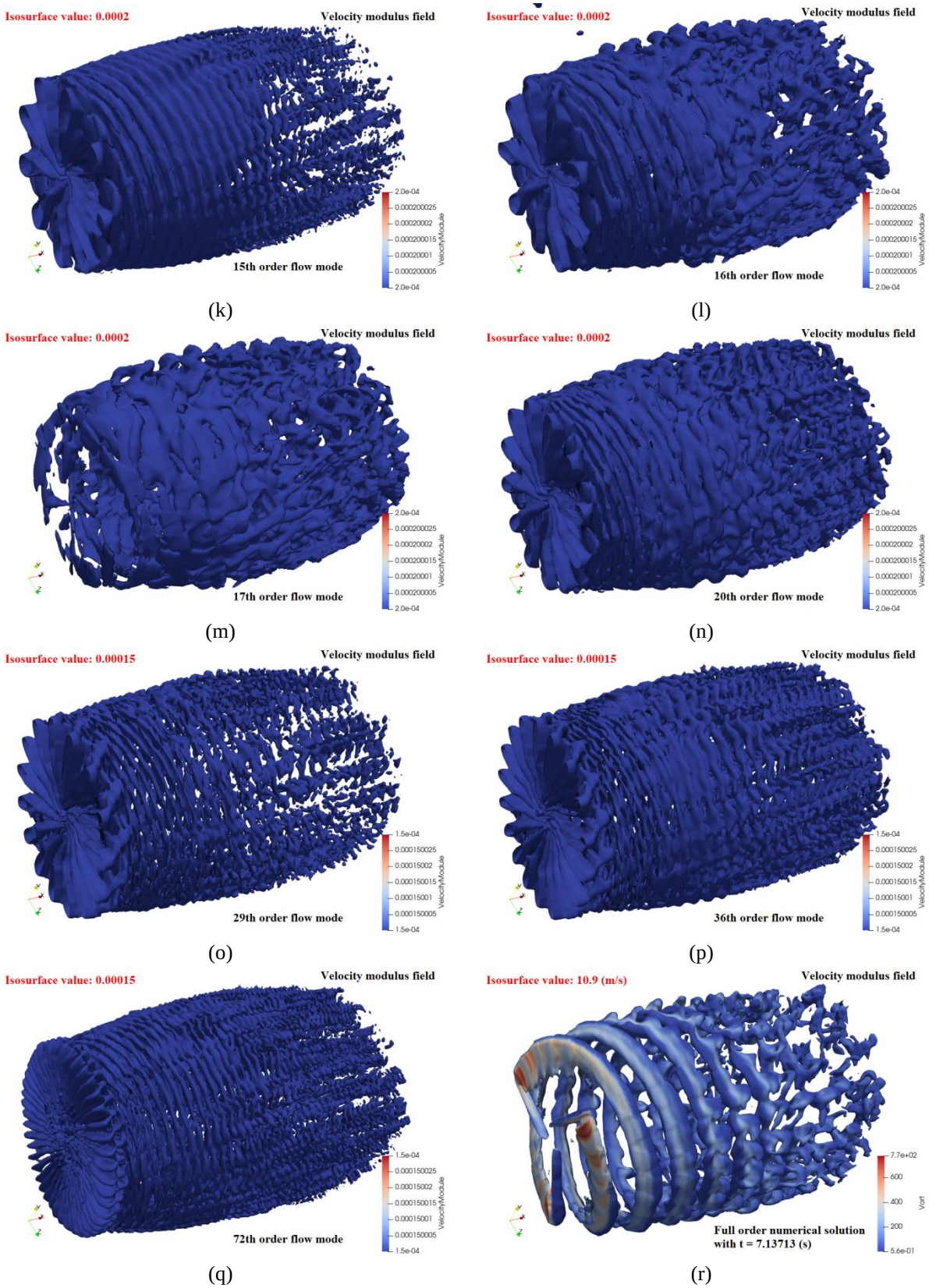

Figure 9: A series of important flow modes of velocity modulus field and the corresponding full-order numerical solution at the specified transient time point: (a) the first-order flow mode, representing the macroscopic average flow; (b) and (c), (f) and (g), (j) - (l), and (n) are the order flow modes projected by tip spiral wake; (d) and (e), (h) and (i) are the order flow modes projected by the X-axial velocity; (m) is the order flow mode projected by a

certain degree of fusion of the tip wake and X-axial velocity; (o) to (q) are the flow modes of corresponding order projected by the deep fusion of the tip wake and X-axial velocity; (r) is the full-order numerical solution of the velocity modulus field at a specified transient time point.

The 1st-order flow mode of tip wake of the velocity modulus field is shown in Figure 9(**a**), with an isosurface value of 0.00055. It is clear that the flow circumferential symmetry at the impeller and near the wake is relatively poor, compared to the corresponding vorticity mode in Figure 8(**a**). The isosurface in Figure 9(**a**) represents the macroscopic average flow.

Figures 9(**c**) and (**d**) show the 2nd-3rd order flow modes of tip wake of velocity modulus field, respectively. Compared with the results in Figures 8 (b), (d), and (v), the spatial distribution frequency of the spiral wake is closest to that of the transient full-order numerical solution in Figure 9(**r**), but the similarity is lower than that of the vorticity field. This indicates that for the velocity modulus field, more flow energy is included in the subsequent high-order modes.

Figures 9(**d**) and (**e**) show the 4th-5th order flow modes. It is distinct that the circumferential random volatility of these two flow modes is strong. Therefore, they are the X-axial velocity modes orthogonal to the blade tip spiral wake.

The 6th-7th order flow modes are the space modes of tip spiral wake shown in Figures 9(**f**) and (**g**). The spatial distribution of the spiral wake is denser. From Figures 9(**h**) and (**i**), it can be seen that they all belong to the space modes dominated by the X-axial velocity.

As shown in Figures 9(**j**) to (**l**), the three modes are typical flow modes dominated by the tip spiral wake. As the modal order increases, the number of local flow structures in the impeller is up to 9. At the same time, the X-axial velocity begins to interfere with the tip spiral wake, which is significant in the spatial dimension of the 16th-order flow mode. As shown in Figure 9(**m**), the mode appears as a fusion flow pattern between the X-axial velocity and tip spiral wake. The 20th mode has a characteristic dominated by tip wakes, where the number of local flow structures in the impeller increases to12.

For the high-order modes in Figures 9(**o**)-(**q**), as the mode order increases, the spatial distribution of the flow characteristic structure in the impeller and tip wake continuously refines. In the 72th-order flow mode, significant circumferential symmetry is maintained, especially near the impeller. The development trend of high-order flow is similar to that of vorticity field modes.

5.1.3 Static pressure field

The third important flow modes of the dimensionless static pressure parameter corresponding to the steady development stage of the impeller wake are shown in Figure 10. Similar to the previous physical parameter fields, the static pressure field modes also from low-to-high order are shown in Figures 10(**a**)-(**o**), and the full-order numerical solution at time point t = 7.13713 (s) is shown in Figure 10(**p**). At the same time, the value of the static pressure isosurface will also change with different modal orders.

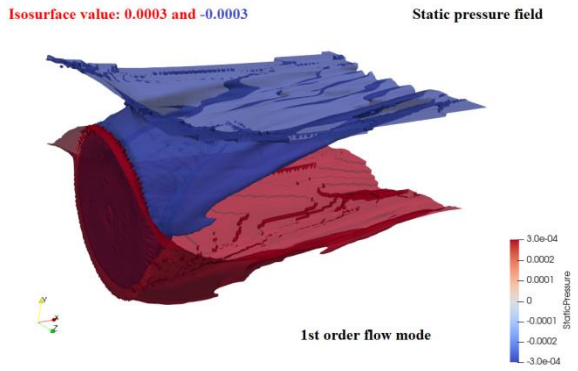

(a)

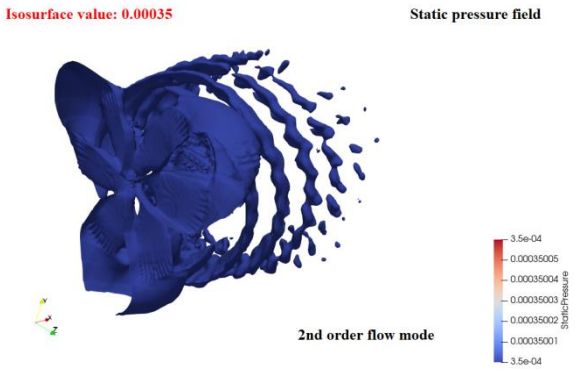

(b)

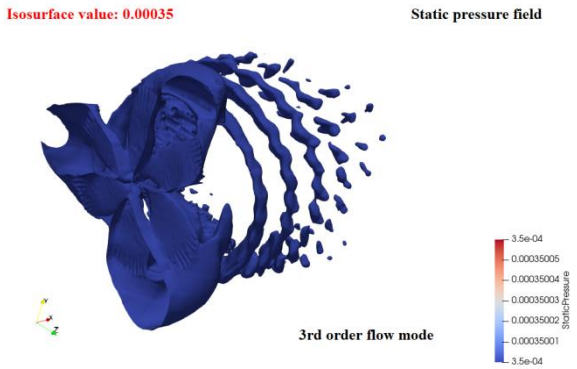
Isosurface value: 0.00035
Static pressure field
3rd order flow mode
3.5e-04
0.00035005
0.00035004
0.00035003
0.00035002
0.00035001
3.5e-04
StaticPressure

(c)

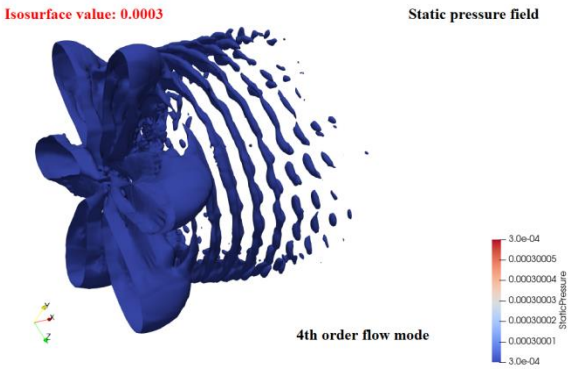
Isosurface value: 0.0003
Static pressure field
4th order flow mode
3.0e-04
0.00030005
0.00030004
0.00030003
0.00030002
0.00030001
3.0e-04
StaticPressure

(d)

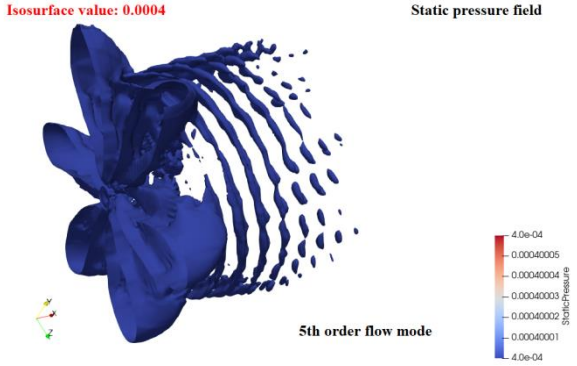
Isosurface value: 0.0004
Static pressure field
5th order flow mode
4.0e-04
0.00040005
0.00040004
0.00040003
0.00040002
0.00040001
4.0e-04
StaticPressure

(e)

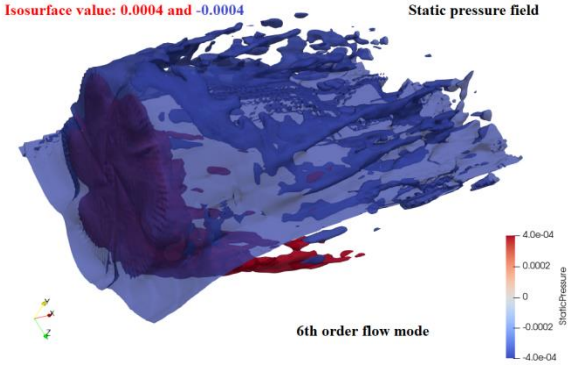
Isosurface value: 0.0004 and -0.0004
Static pressure field
6th order flow mode
4.0e-04
0.0002
0
-0.0002
-4.0e-04
StaticPressure

(f)

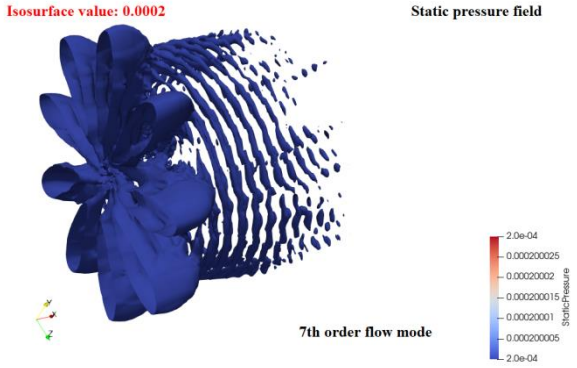
Isosurface value: 0.0002
Static pressure field
7th order flow mode
2.0e-04
0.000200025
0.00020002
0.000200015
0.00020001
0.000200005
2.0e-04
StaticPressure

(g)

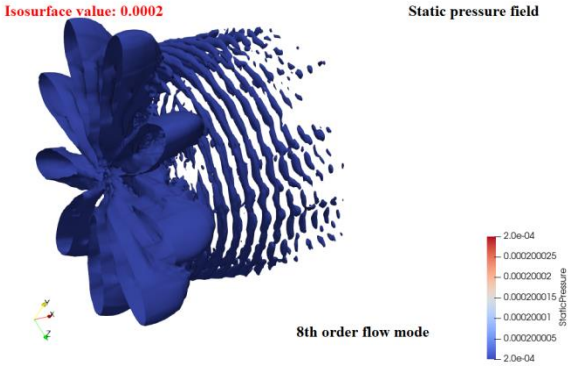
Isosurface value: 0.0002
Static pressure field
8th order flow mode
2.0e-04
0.000200025
0.00020002
0.000200015
0.00020001
0.000200005
2.0e-04
StaticPressure

(h)

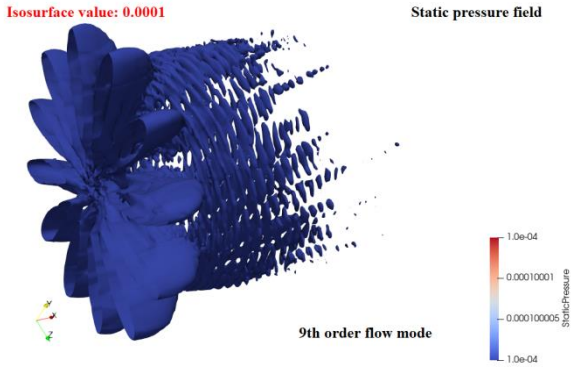
Isosurface value: 0.0001
Static pressure field
9th order flow mode
1.0e-04
0.00010001
0.000100005
1.0e-04
StaticPressure

(i)

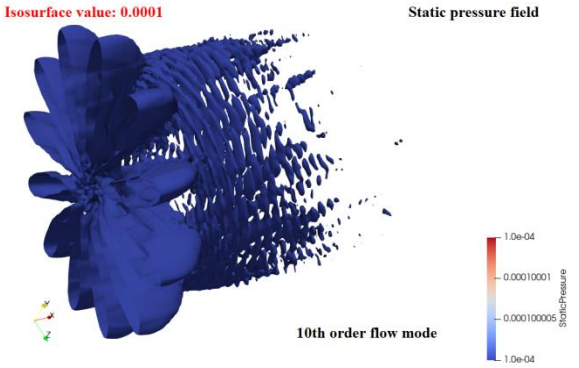
Isosurface value: 0.0001
Static pressure field
10th order flow mode
1.0e-04
0.00010001
0.000100005
1.0e-04
StaticPressure

(j)

International Journal of Multiphysics
Volume 18, No. 2s, 2024
ISSN: 1750-9548

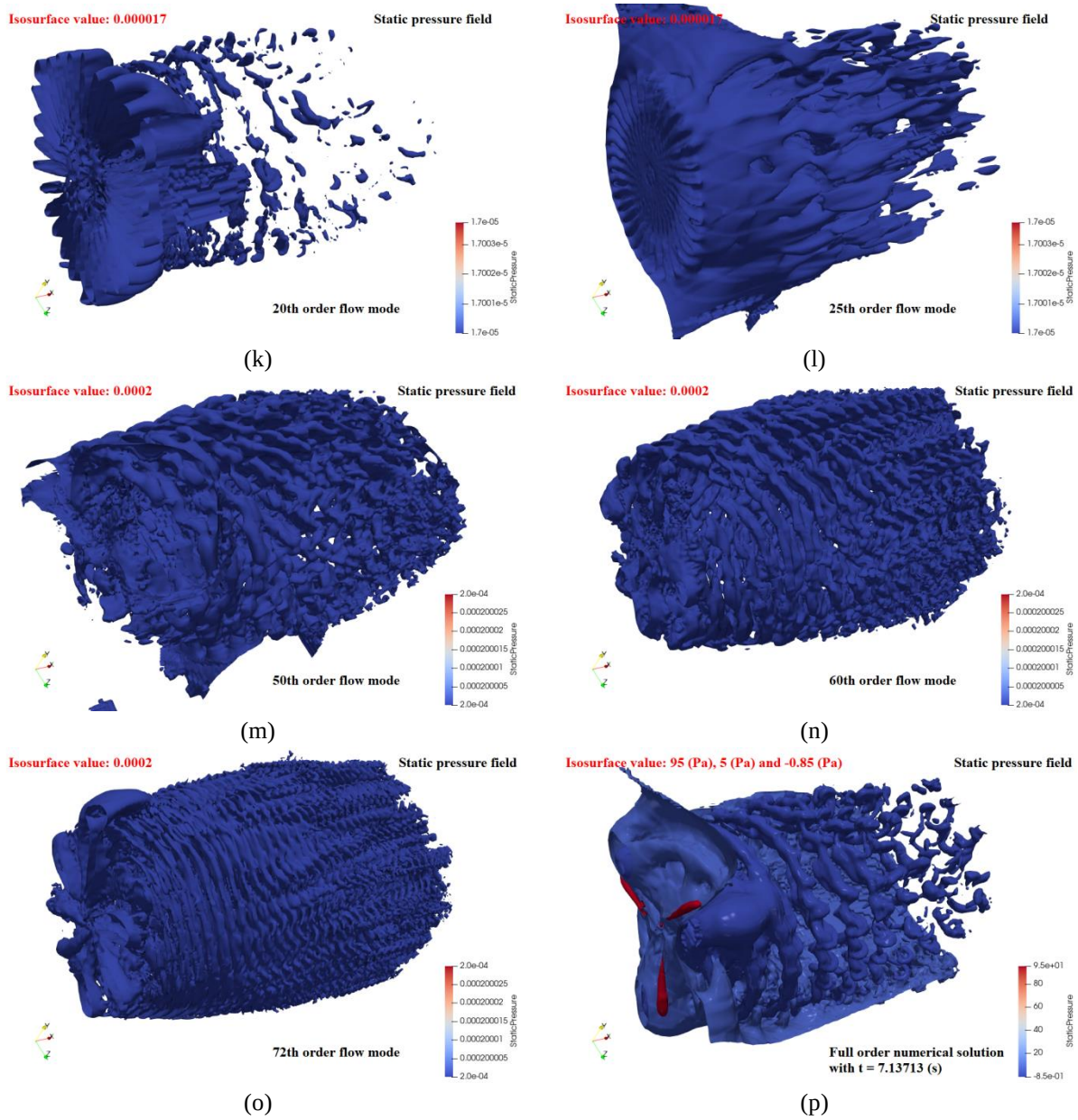

Figure 10: A series of important flow modes of the static pressure field and the full-order numerical solution at a specified transient time point: (a) is the first-order flow mode, representing macroscopic average flow; (b) - (e), (g)- (j) are the orderflow modes projected by the impeller surface flow and tip spiral wake; (f) is the order flow mode projected by the disturbing flow rooting in these specific physical boundary and working conditions; (k) and (l) are the order flow modes projected by the impeller surface flow and tip spiral wake with enhanced volatility; (m) and (n) are the order flow modes projected by the impeller surface flow and tip spiral wake, with more energy information in the wake; (o) is the order flow modes projected by the deep fusion of circumferential distribution and random volatility; (p) is the full-order numerical solution of the static pressure field at a specified transient time point.

As shown in Figure 10(**a**), the isosurface values for the 1st-order flow mode of the tip wake of the static pressure field are in the range of 0.0003 and -0.0003. The pressure and suction surfaces of the impeller rotating plane represent the relative positive pressure (red color) and negative pressure (blue color), respectively. It just shows the conditions necessary for the wind turbine impeller to generate aerodynamic torque in an overall sense. The

two positive and negative static pressure isosurfaces in the wake indicate that the central region of the impeller wake is in a low-pressure state, and there is a significant velocity deficit in the central wake.

From the 2nd-5th order flow modes in Figures 10(**b**) to (**e**), as well as the 7th-10th order modes in Figures 10(**g**) to (**j**), a localflow structure with circumferential symmetry can be seen at the impeller. As the mode order increases, the number of local flow structure increases by a multiple of 3, which is the physical number of blades of the impeller. This change law is also reflected in the vorticity field and velocity modulus field discussed earlier. At the same time, as the mode order increases, the spiral structure of the tip wake is continuously refined, and the circumferential random fluctuation characteristics of the spiral wake are gradually enhanced, especially the 9th and 10th orders.

In Figure 10(**f**), the 6th-order flow mode further complicates the spatial distribution pattern of the rotational wake flow field, which is closely related to specific physical problems and operating conditions. For the 20th-order mode in Figure 10(**k**), the local flow structure has obvious random fluctuation characteristics, corresponding to the impeller region. For the 25th-order mode in Figure 10(**l**), the energy information in the wake begins to increase, and the randomness of the overall flow pattern also increases.

For the 50th and 60th-order modes in Figures 10(**m**) and (**n**), the main flow energy information is reflected in the wake flow field. For the 72th-order mode in Figure 10(**o**), the characteristics of the circumferential distribution and random volatility of the impeller and tip spiral wake is in a deep fusion state. In addition, the development trend of high-order flow modes is similar to the modes of vorticity field and velocity modulus field discussed earlier. The deep fusion stage reflects the quasi-resonance mechanism of the local wake flow structure of the blade tip vortexs.

5.2 Energy Content of Flow Modes

According to the definitions of Eqs. (12) and (13) based on the Sirovich-DPOD method in Section 2, the energy content ratios of 241 spatial modes of the tip wake flow field of the rotating impeller are quantified. The spectrum curves for the energy content are shown in Figure 11.

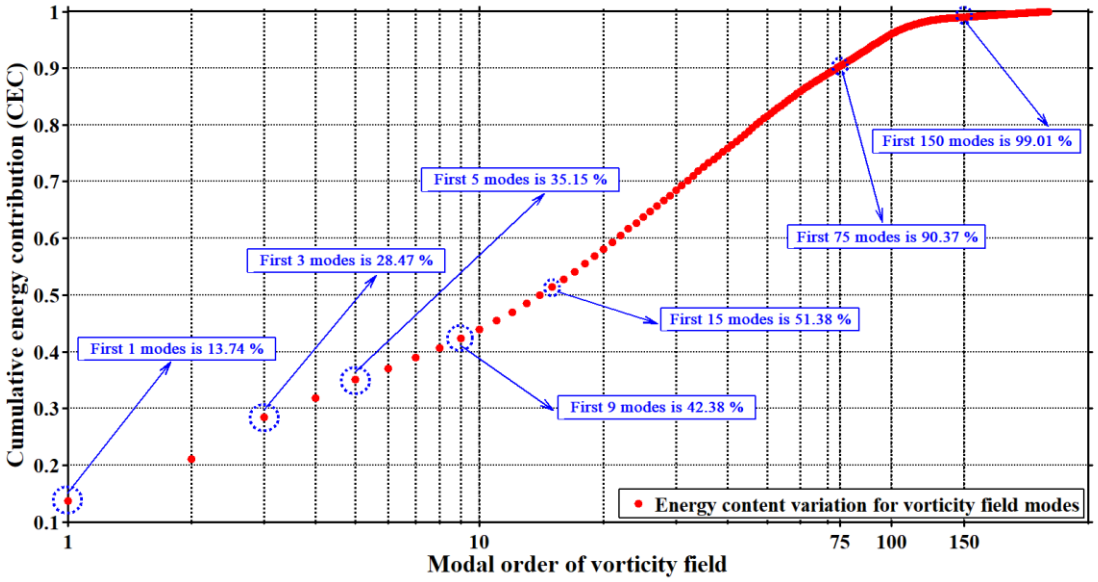

(a)

International Journal of Multiphysics
Volume 18, No. 2s, 2024
ISSN: 1750-9548

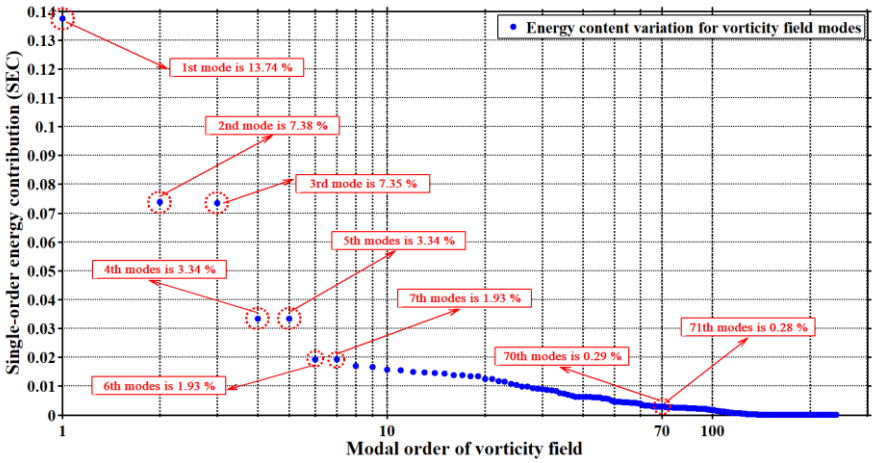

(b)

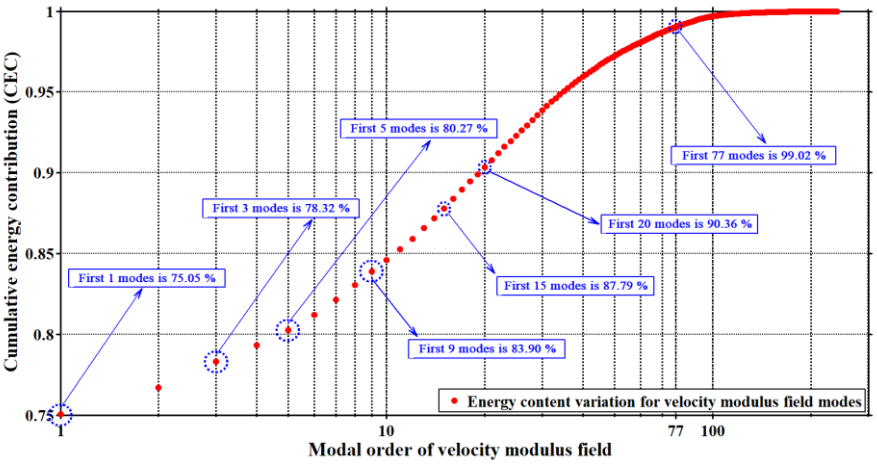

(c)

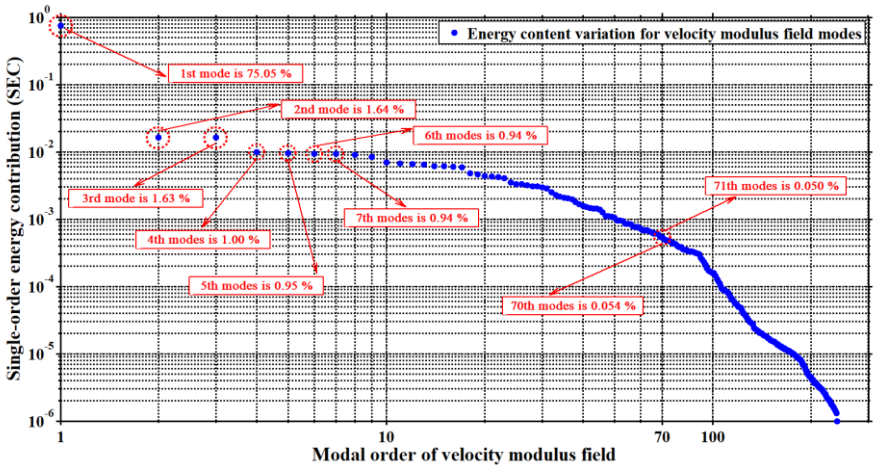

(d)

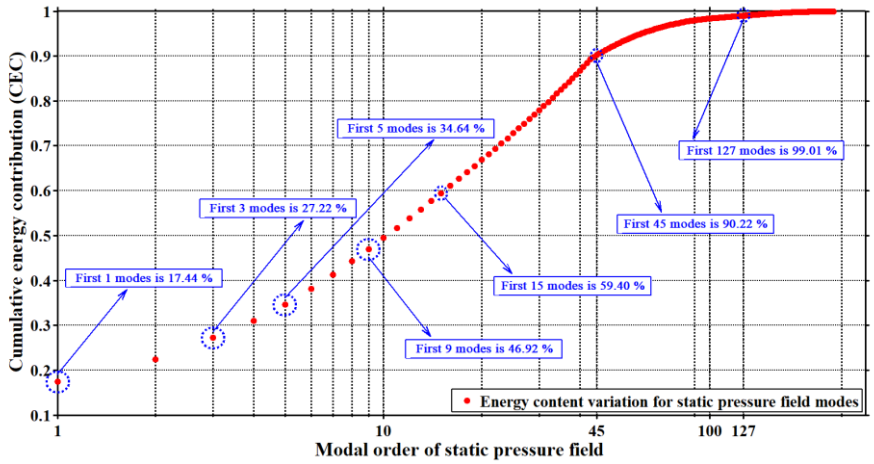

(e)

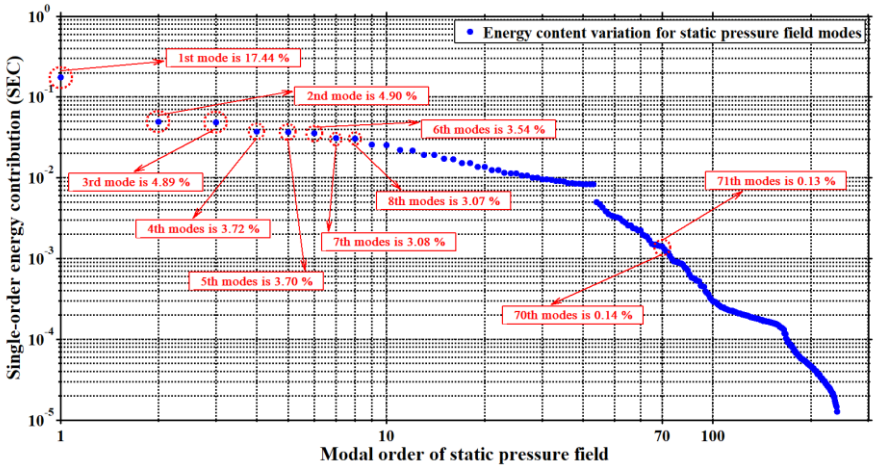

(f)

Figure 11: Variations in the energy content spectrum curve of the physical parameter fields of the impeller wake: (a) and (b) are the CEC and SEC of vorticity field modes; (c) and (d) are the CEC and SEC of velocity modulus field modes; (e) and (f) are the CEC and SEC of static pressure field modes.

Figures 11(**a**) and (**b**) show the energy variations of the CEC and SEC of vorticity field modes, respectively. The overall spectral characteristics indicate that the energy proportion of the first mode is 13.74%, as shown in the macroscopic average flow in Figure 8(**a**). The energy contents in the first 9-order and the first 15-order flow modes are 42.38% and 51.38%, respectively. For the first 75-order and first 150-order modes, the energy content proportion is up to 90.37% and 99.01%, respectively. The variation reflects a certain degree of energy content dominant characteristics in low order modes, providing a clear quantitative basis for determining the important vortex structures in the complex wake of rotating impellers.

Another phenomenon that attracts great attention is that for the 2nd and 3rd-modes, 4thand 5th-modes, 6thand 7th-modes, and more, based on theoretical considerations, the SEC levels of these two modes should be completely equal. The corresponding spatial morphology can refer to Figures 8(**b**) and (**c**), Figures 8(**d**) and (**e**), Figures 8(**f**) and (**g**), and more. Their characteristics have a little difference due to the error of numerical calculation. It is also implied that some important localization characteristics of the vorticity field of the rotating impeller wake are determined by these two associated modes. Figures 11(**c**) and (**d**) shows the energy content variations of the CEC and SEC of the velocity modulus field modes, respectively. Figures 11(**e**) and (**f**) show the energy content variations of the CEC and SEC of static pressure field modes, respectively. It can be seen that the variation trend and characteristics of the modes of these latter two physical parameter fields are similar to the wake vorticity field. Among them, the energy content characteristics of the wake velocity modulus field at

the low-order modes are more obvious than those of the vorticity field and static pressure field. Therefore, for the velocity physical parameter field, it is more suitable to establish a high-precision low-order model for the impeller rotating wake flow.

5.3 Time-frequency Response

According to the study on the energy content ratio of flow modes, the SEC level of low-order modes is relatively high. In terms of Sirovich-DPOD algorithm, the influence of flow modes on the overall flow rate is proportional to the value of SEC. Hence, the time coefficients of the first 15 order flow modes are selected as the research objects. In the process, the fast Fourier transform (FFT) algorithm is used to obtain the time-frequency domain variation characteristics of the time.

5.3.1 Time-domain

The time-domain responses to the time coefficients of the first 71 modes of the vorticity field are shown in Figure 11, except for the 1st flow mode that will be discussed separately later. In Figure 12(**a**), combined with the results in Figure 8, the time-domain variation characteristics of the time coefficients of the 2nd -7th modes dominated by tip wake are presented. The 2nd and 3rd order time coefficients have almost identical harmonic variations with the same amplitude, and there is only a constant difference between the phases. The 4th and 5th orders, 6th and 7th orders also have similar regularity.

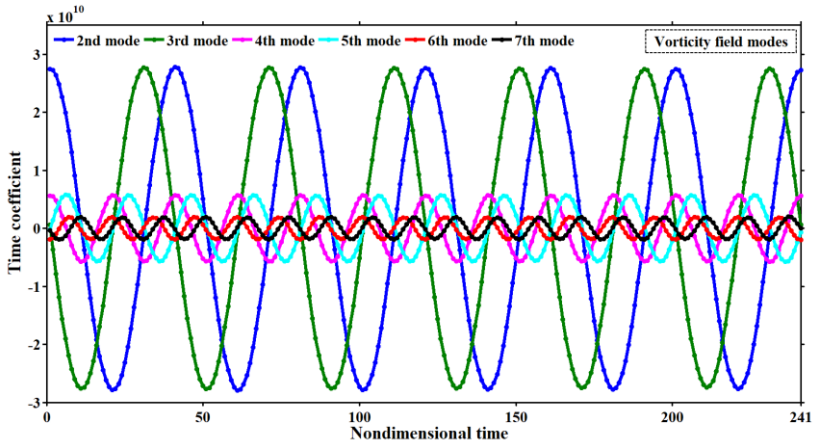

(a)

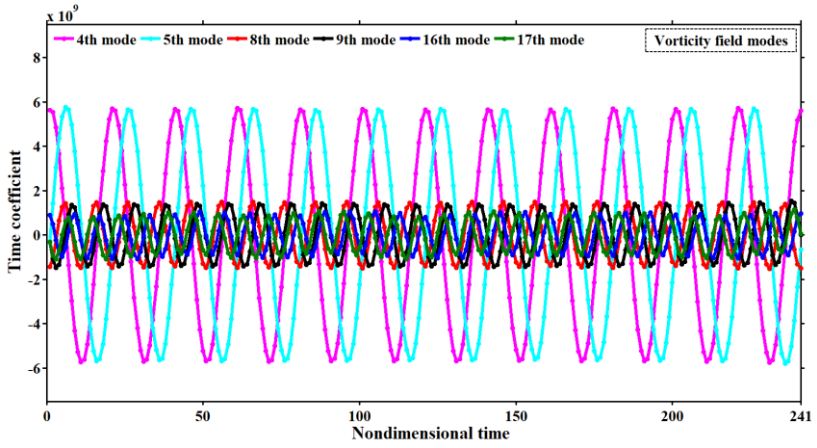

(b)

International Journal of Multiphysics
Volume 18, No. 2s, 2024
ISSN: 1750-9548

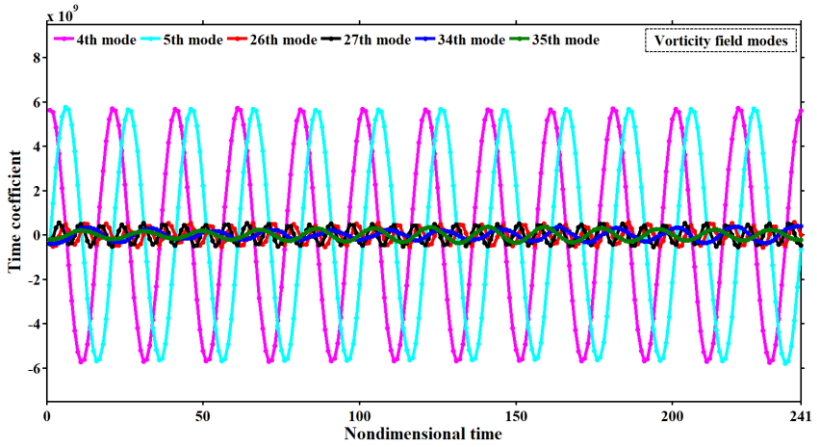

(c)

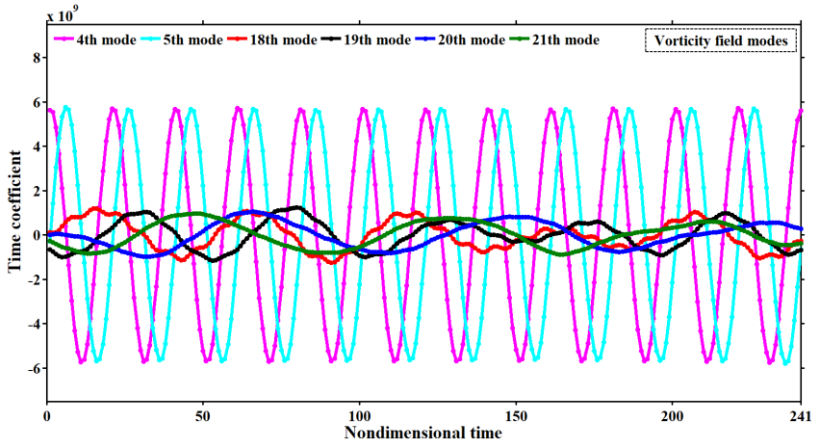

(d)

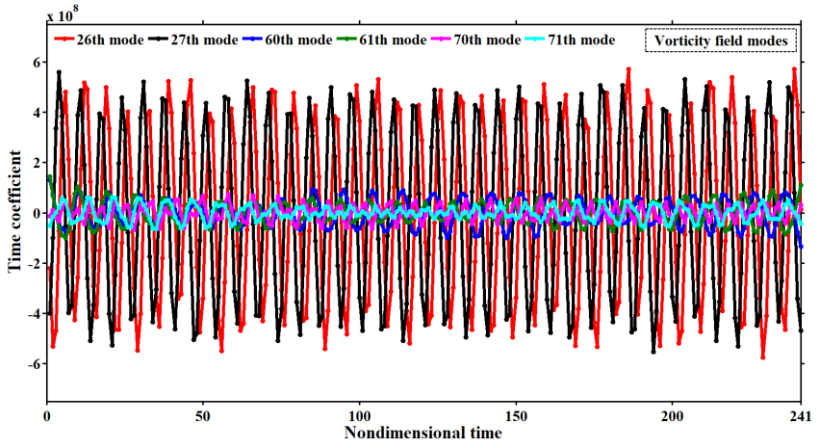

(e)

Figure 12: The time-domain variation characteristics of the time coefficients of a series of flow modes in the vorticity field: (a) and (b) are the time coefficients of flow modes of the order projected by blade tip spiral wake;(c) and (d) are the contrasts of time coefficients of the order flow modes projected by blade surface attached vortex wake and blade tip spiral wake; (e) is a comparison of the time coefficients of the orderflow modes projected by the deep fusion of the tip vortex and attached vortex.

However, due to the increase in modal order in the wake, the amplitude of the time coefficients corresponding to the 4th and 5th orders, as well as the 6th and 7th orders increases gradually. Meanwhile, the difference in the corresponding phases gradually decreases from the 2nd-3rd orders to 6th-7th orders. The high-order modes

dominated by tip wake also have similar characteristics, as shown in Figure 12(**b**). As the mode orders increase and the energy content decreases, the identical harmonic characteristics of the time coefficients of high-order flow modes projected by the tip wake have significant local random fluctuation, as shown in Figure 12(**e**).It is significantly affected by the attached vorticity detached from the blade surface and the incoming flow.

On the contrary, the high-order flow modes projected by the attached vorticity are also affected by the tip spiral wake. As such, their time coefficients have certain harmonic characteristics in the time-domain, as shown in Figure 12(**d**). Specially in Figure 12 (c), there is a stark contrast between the 4th-5th orders dominated by the tip wake and the 34th-35th orders projected by attached vorticity. In the representative modes of the velocity modulus field and the static pressure field, the time-domain responses of the time coefficients are shown in Figures 13 and 14, respectively, with the exception of the first flow mode, which will be discussed later. The variation law of the time coefficients of these two fields is basically consistent with the characteristics of the vorticity field.

In Figure 13(**a**), combined with the results in Figure 8, the flow modes dominated by the tip vortex are the 2nd and 3rd, 6th and 7th, 14th and 15th and 16th, respectively. The variation of the time coefficients in the 6th and 7th orders is no longer the same harmonic mode. The center of the harmonic variation is no longer a horizontal straight line, but with a certain change of the curve.

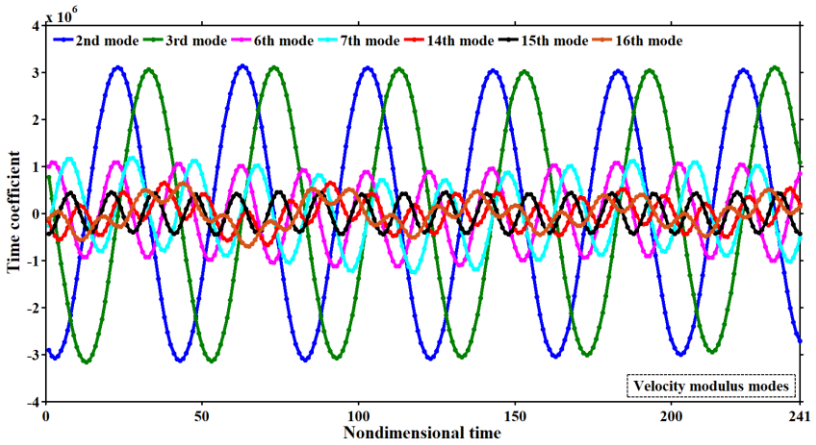

(a)

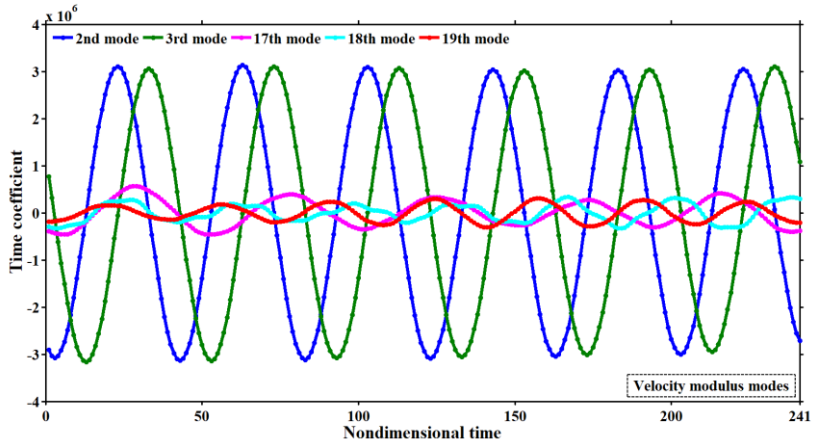

(b)

Figure 13: The time-domain variation characteristics of the time coefficients for a series of flow modes of the velocity modulus field: (a) is the time coefficients of the order flow modes projected by the tip spiral wake; (b) is a comparison of the time coefficients of the order flow modes projected by the X-axial velocity wake and tip spiral wake.

International Journal of Multiphysics
Volume 18, No. 2s, 2024
ISSN: 1750-9548

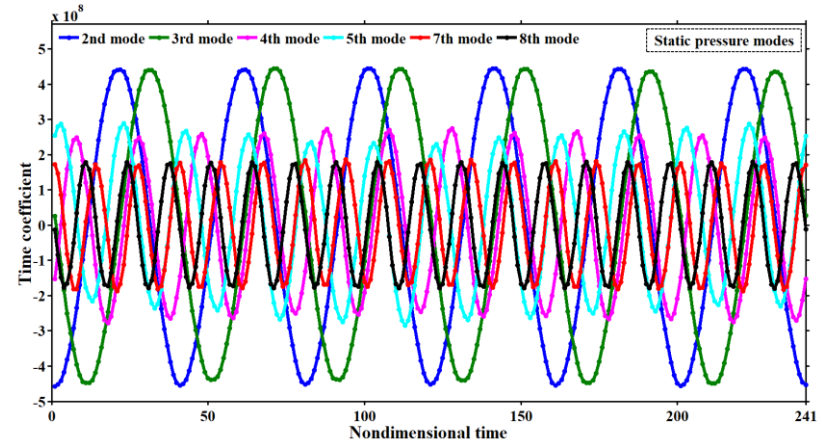

(a)

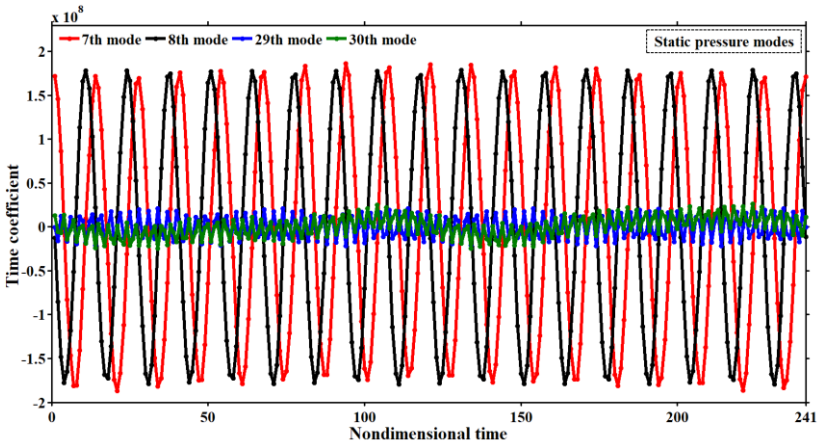

(b)

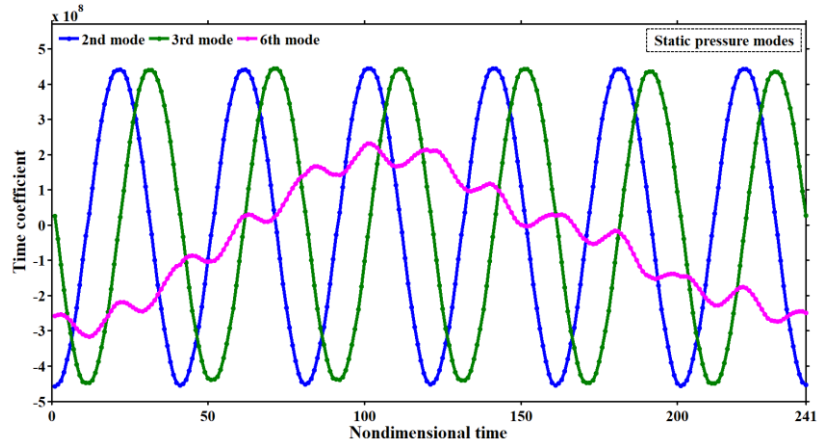

(c)

Figure 14: The time-domain variation characteristics of the time coefficients of a series of flow modes in the static pressure field: (a) is the time coefficients of the orderlow modes projected by blade tip wake; (b) is a comparison of the time coefficients of the orderflow modes projected by the tip wake and the deep fusion wake; (c) is a comparison of the time coefficients of the order flow modes projected by the X-axial velocity wake and the tip spiral wake.

The time-domain coefficients of the first mode of the three physical parameter fields of vorticity, velocity modulus and static pressure are shown in Figure 15. The 1st-order time coefficients of the vorticity and velocity modulus are characterized by horizontal straight lines, represented by the red and blue lines. This indicates that

in the time domain propulsion, the global average flow of the vorticity and velocity modulus fields are approximately stable. On the contrary, the first-order static pressure time coefficient fluctuates significantly, indicating that the low-order flow of static pressure field is more variable than the vorticity field and the velocity modulus field. It should be noted that only the same type of flow parameters are comparable at the numerical level, while the numerical comparison of different types of flow parameters cannot be carried out directly.

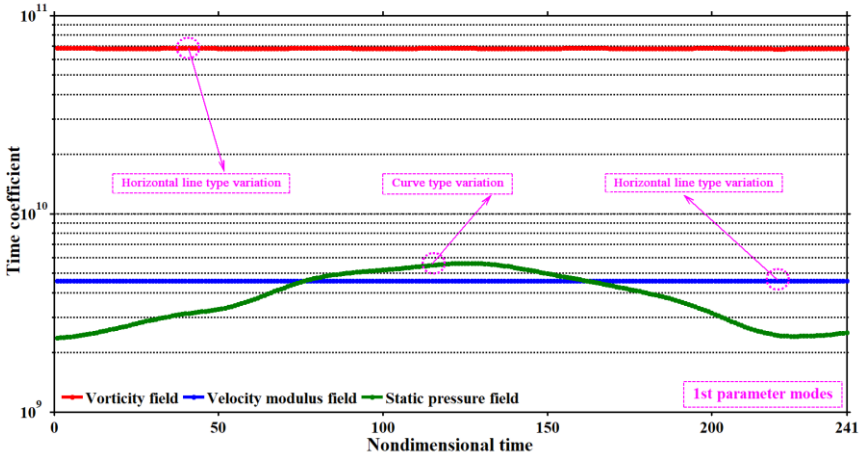

Figure 15: Time-domain response of the first-order time coefficients in different physical fields

5.3.2 Frequency domain

The frequency-domain characteristics of the time coefficients of the first 71 modes in the vorticity field are shown in Figure 16, except for the 1st flow mode. In Figure 16(**a**), the 2nd-3rd modes, 4th and 5th modes, 6th and 7th modes, and 8th and 9th modes all have the same frequencies and amplitudes.

The specific physical flow modes in Figures 8(**b**) to (**i**) indicates that a series of modes mainly from the energy mapping of the impeller tip spiral wake. At the same time, combined with the design speed of the wind turbine, the peak frequencies of the 2nd and 3rd orders of the rotational fundamental frequency of the tip spiral wake are 37.36 Hz. In addition, the peak frequencies of the 4th- 9th order modes are high multiple frequencies of the tip wake mappings, which are two to four times the fundamental frequency. This is similar to the frequency spectrum variation of structural vibrations, where the amplitude of high-order frequencies decreases as the modal order increases.

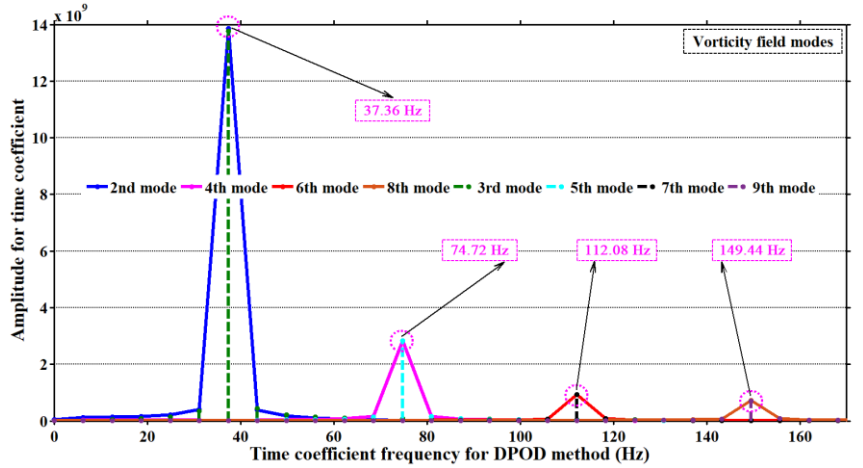

(a)

International Journal of Multiphysics
Volume 18, No. 2s, 2024
ISSN: 1750-9548

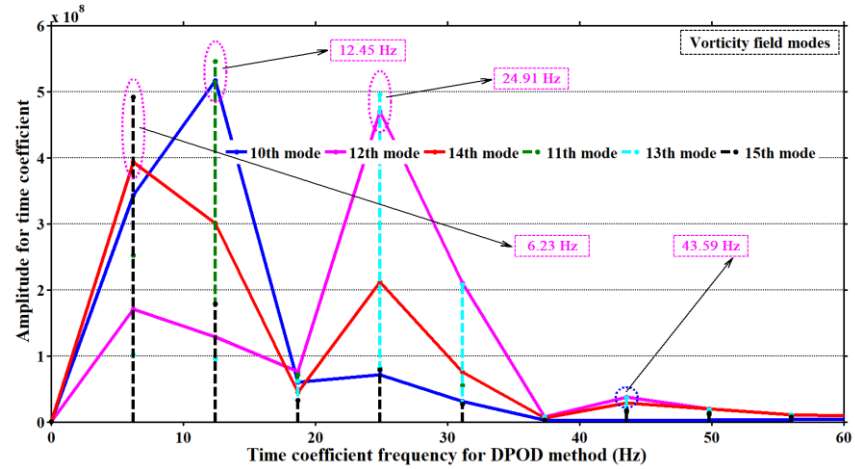

(b)

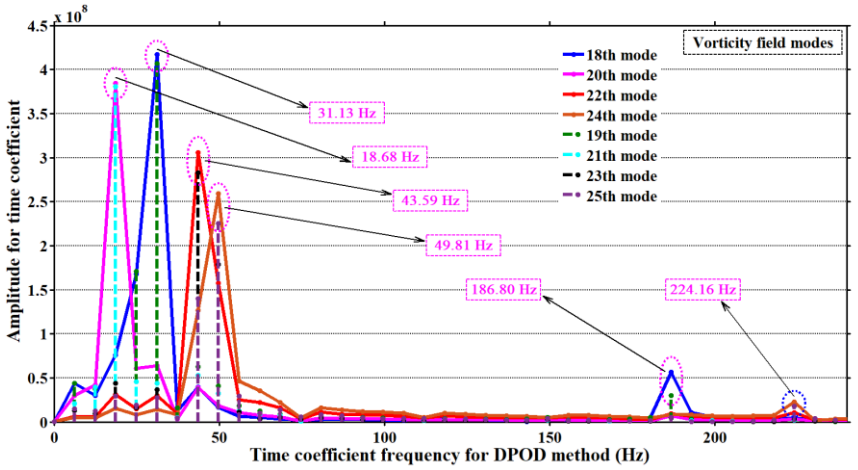

(c)

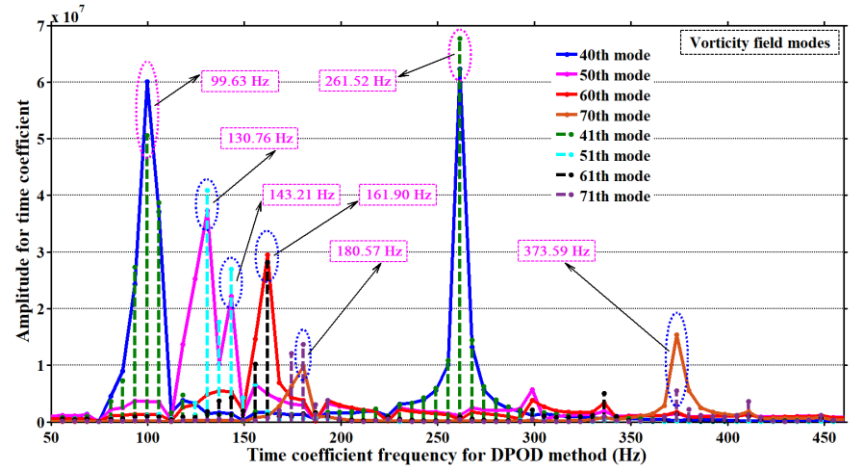

(d)

Figure 16: The frequency-domain variations of the time coefficients for a series of flow modes of the vorticity field: (a) is the time coefficients of the order flow modes projected by the blade tip spiral wake; (b) is the time coefficients of the order flow modes projected by the blade surface attached vortex wake; (c) is a comparison of time coefficients of the order flow modes projected by the blade surface attached vortex wake and the blade tip spiral wake; (d) is a comparisons of time coefficients of the order flow modes projected by the deep fusion of the tip vortex and attached vortex.

As shown in Figure 16(**a**), as the modal order increases, the amplitudes of the series peak frequencies all decreases, and the equal amplitude characteristics of the bimodal common frequency slightly change. Therefore, the energy mapping is affected by the wake of the attached vortexes detached from the blade surface. As shown in Figure 16(**b**), the constant amplitude changes significantly, with the lowest peak frequency dropping to 6.23 Hz. This is because the projected energy mainly comes from the detached attached vortex structure, as shown in Figures 8(**j**) to (**o**). As shown in Figure 16(**c**), the mapping of attached vortex wakes of the order modes is also affected by the tip wake. As shown in Figure 16(**d**), the mapping of the attached vortex and tip vortex enters into a deep fusion state. In addition to the change of constant amplitude characteristics, the two frequency components of approximate amplitude appear in the same mode, such as the 40th mode. The velocity modulus field and static pressure field of the first 72 modes are shown in Figure 17 and Figure 18, respectively, except for the 1st flow mode. For these two fields, the variation law of frequency domain characteristics is basically similar to that of the vorticity field. As shown in Figure 17(**a**), the equiamplitude characteristics of the 6th and 7th modes projected by the tip wake begin to change. For the14th, 15thand 16th flow modes, the difference is even more pronounced.

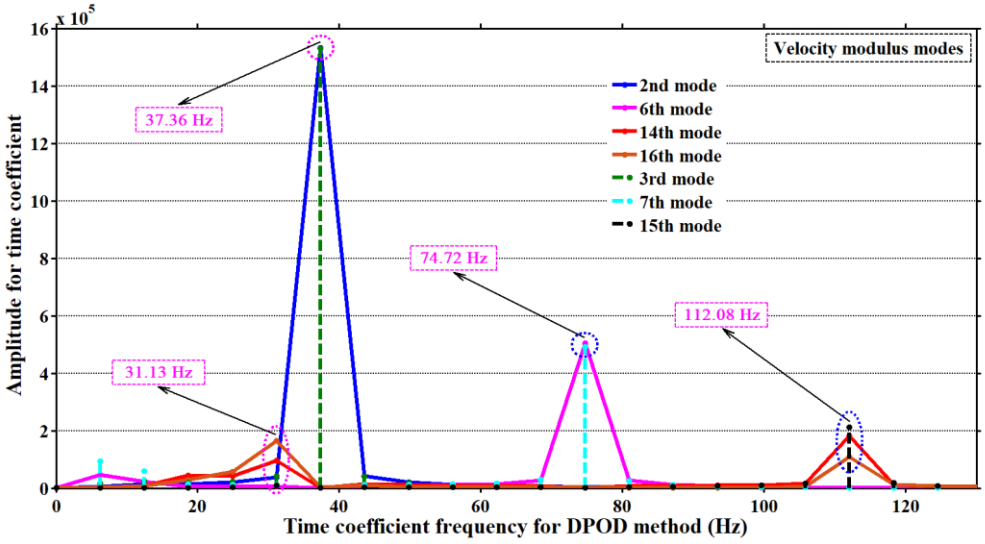

(a)

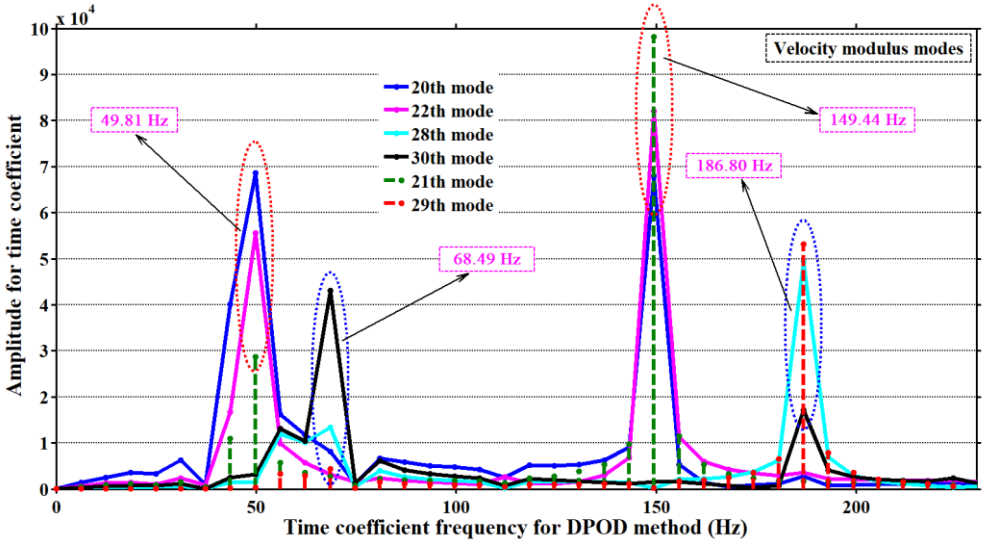

(b)

International Journal of Multiphysics
Volume 18, No. 2s, 2024
ISSN: 1750-9548

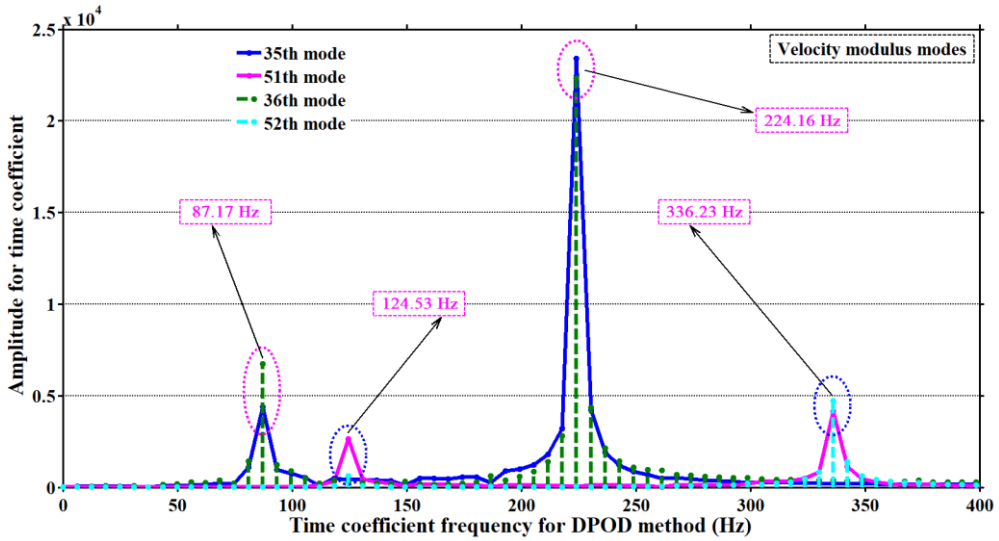

(c)

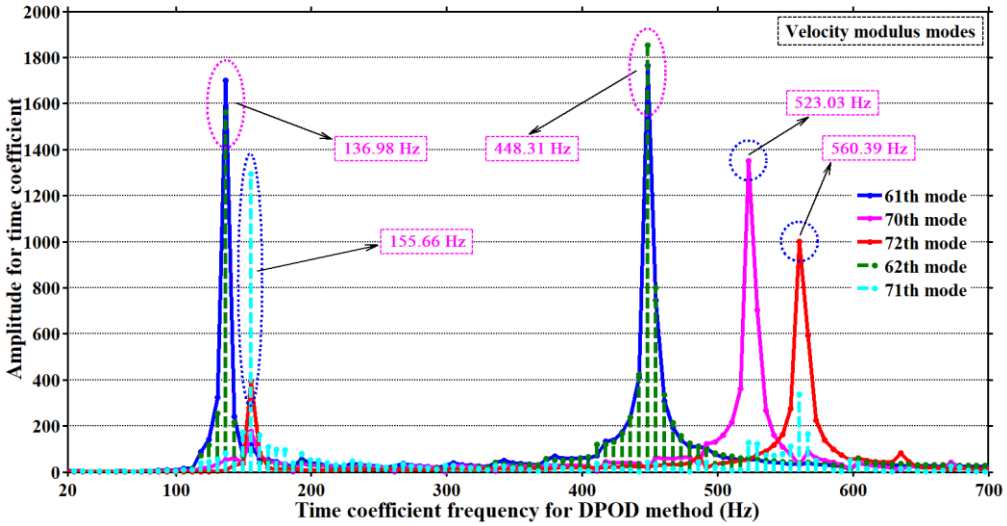

(d)

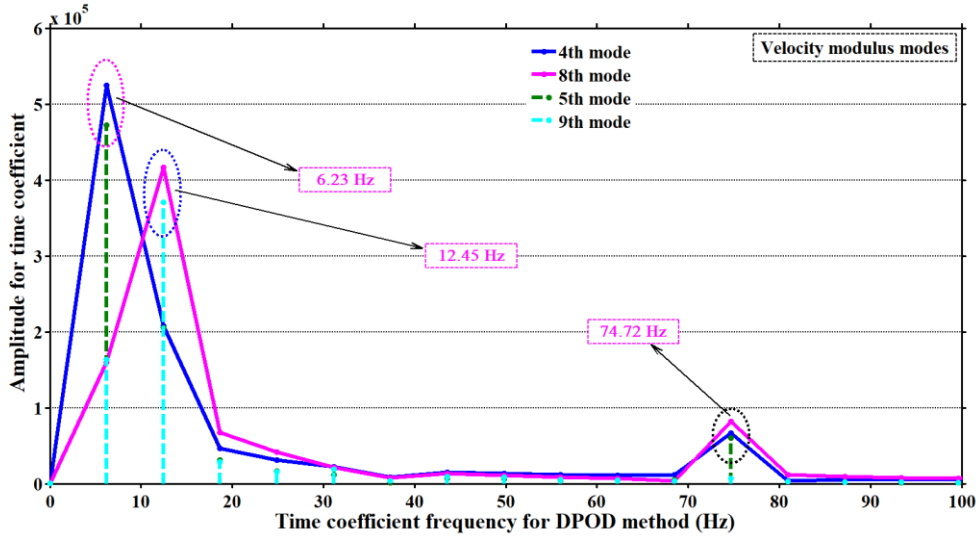

(e)

International Journal of Multiphysics
Volume 18, No. 2s, 2024
ISSN: 1750-9548

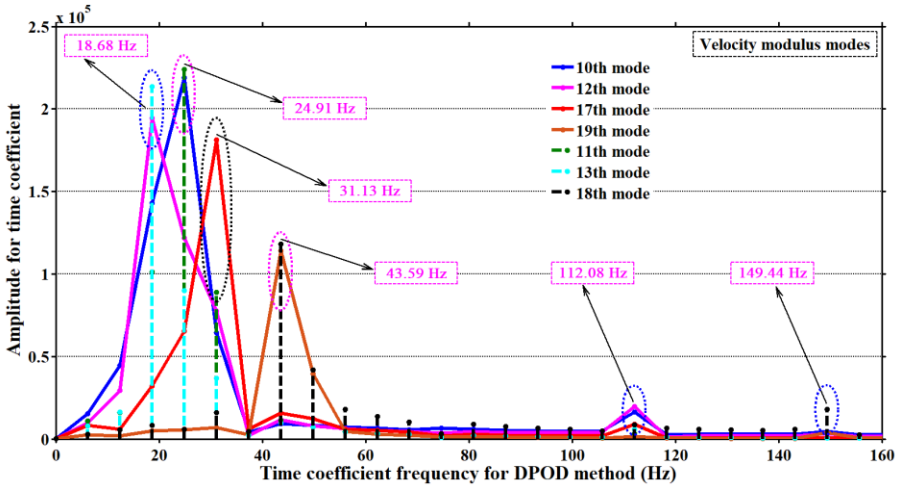

(f)

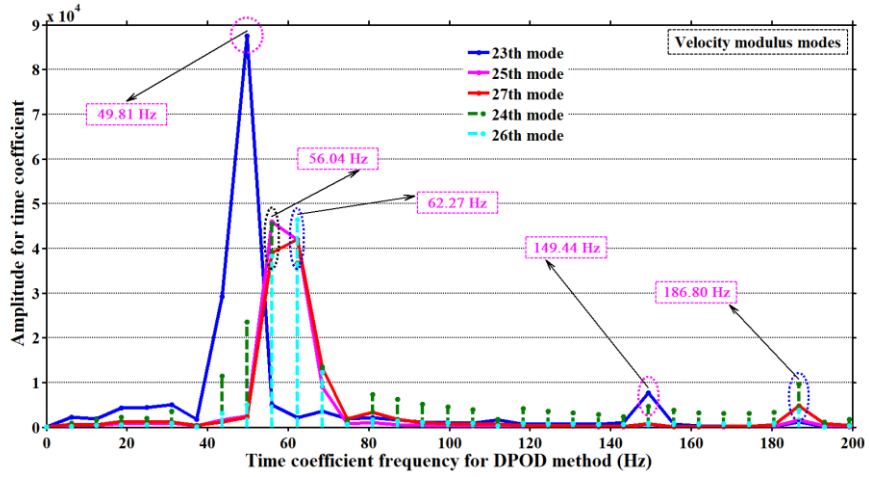

(g)

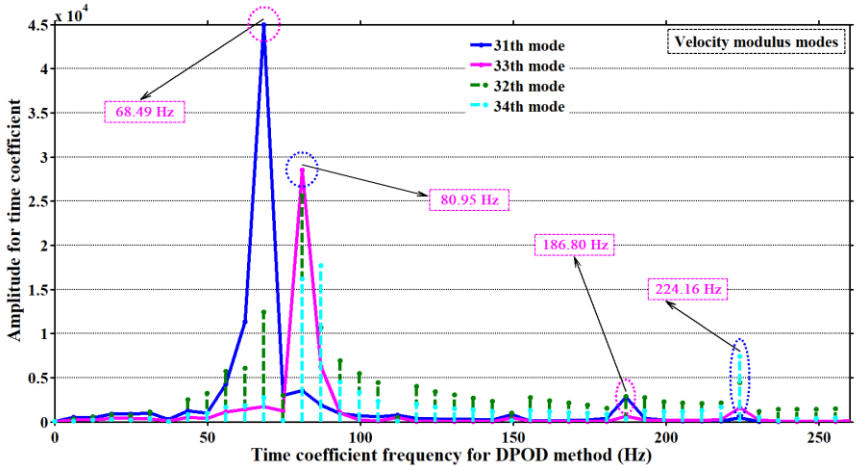

(h)

Figure 17:The frequency-domain variation characteristics of the time coefficients for a series of flow modes of the velocity modulus field: (a) is the time coefficients of the orderflow modes projected by the blade tip spiral wake; (b), (f), (g), and (h) are a comparison of time coefficients of the orderflow modes projected by the X-axial velocity wake and tip spiral wake; (e) is a comparison of the time coefficients of the orderflow modes projected by the X-axial velocity wake; (c) and (d) are a comparison of the time coefficients of the orderflow modes projected by the deep fusion of the tip wake and X-axial velocity.

International Journal of Multiphysics
Volume 18, No. 2s, 2024
ISSN: 1750-9548

Compared with the vorticity field and velocity mode field, the same frequency and amplitude extend to a high-order mode space, as shown in Figures 18(**a**) to (**c**), especially with a series of high-frequency components applied in the 17th-24th order modes in Figure 18(**c**). Meanwhile, the difference in peak frequency between the modes projected by the X-axial velocity wake and tip wake is more significant, such as the 25th mode in Figure 18(**d**), and Figure 10(**l**).

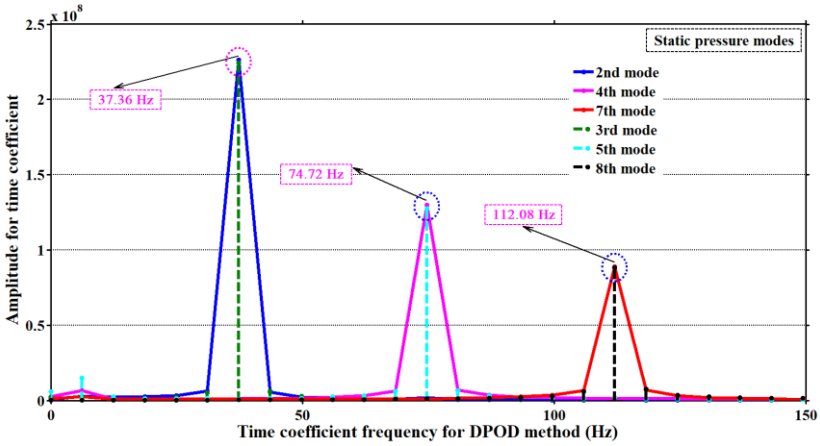

(a)

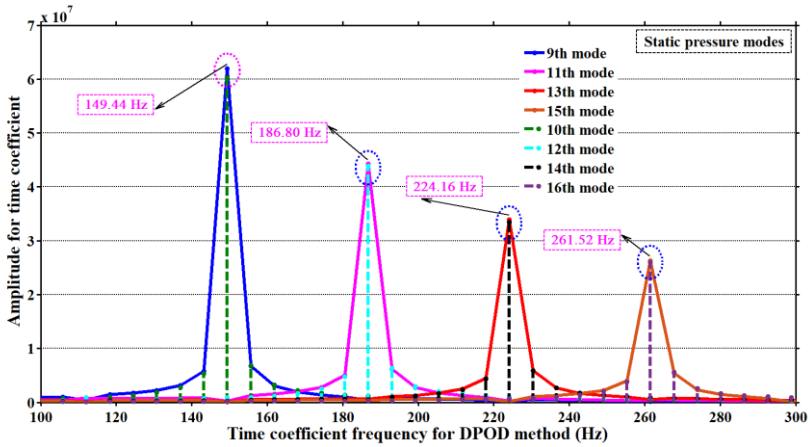

(b)

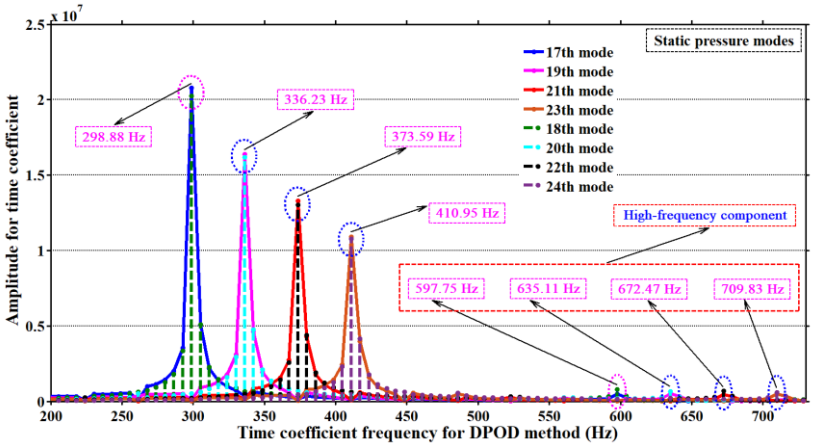

(c)

International Journal of Multiphysics
Volume 18, No. 2s, 2024
ISSN: 1750-9548

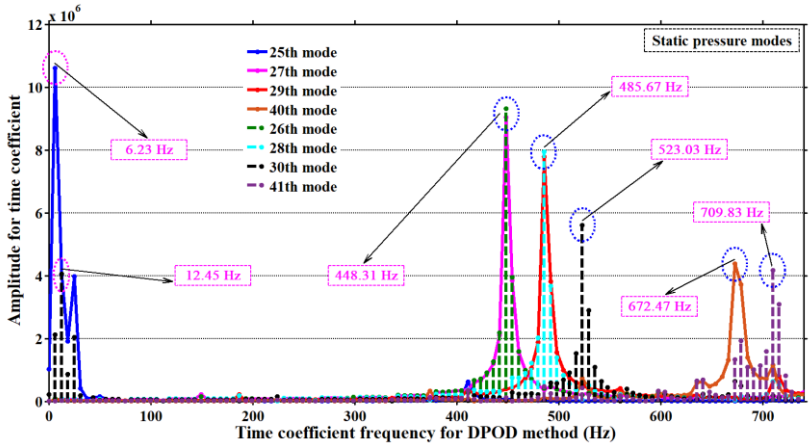

(d)

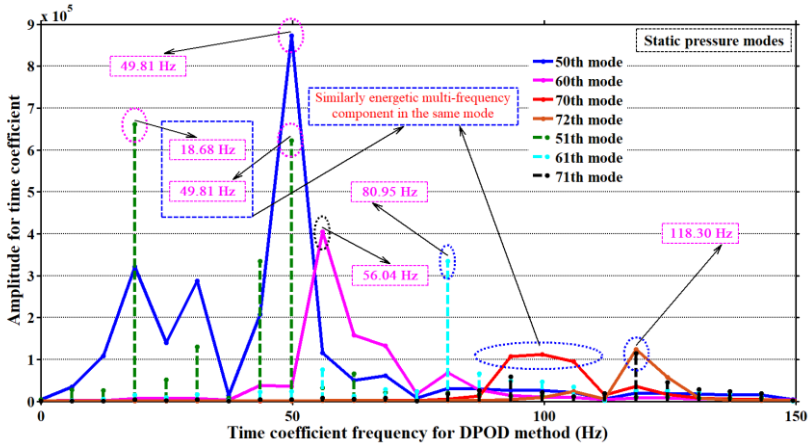

(e)

Figure 18: The frequency-domain variation characteristics of the time coefficients for a series of flow modes of the static pressure field: (a) - (c) are the time coefficients of the orderflow modes projected by the tip wake; (d) is a comparison of time coefficients of the orderflow modes projected by the X-axial velocity wake and tip wake; (e) is a comparison of time coefficients of the orderflow modes projected by the deep fusion of the tip wake and X-axial velocity.

The frequency-domain time coefficients of the 1st-mode in the three physical parameter fields of vorticity, velocity modulus and static pressure are shown in Figure 19. The maximum peak frequencies of the 1st-order modes of the three physical parameter fields are all zero. This indicates that most of the energy content of the 1st order modes are the macro average flow.

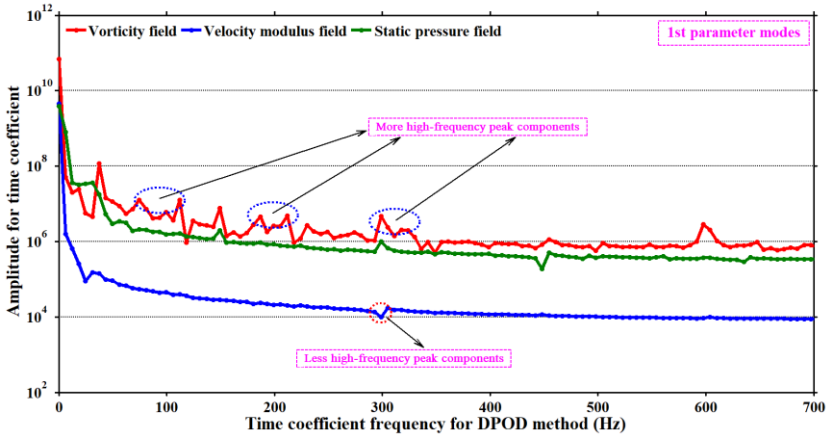

Figure 19: Frequency-domain response of the first-order time coefficients of different physical fields

In addition, the 1st-order mode of the vorticity field contains more high-frequency peak components than the velocity mode and static pressure field, indicating that the localized complex flow in the vorticity field has a higher energy level. Compared with the velocity modulus and static pressure field, the high-order vortex structure in the vorticity field has a more significant impact on the tip spiral wake.

6 CONCLUSION

A methodology based on the Sirovich DPOD algorithm is proposed to resolve the multilevel complicated rotational flow wake of the wind impeller. A discrete strategy is used to determine the key 3D sub-region to achieve data structure homology and reduce calculation. The LBM-LES turbulence model, the wall-adapting local eddy viscosity model, and the D3Q27 model are also used in the study.

The results show that the 1st-order flow modes of the three physical parameter fields of vorticity, velocity modulus and static pressure, have the macroscopic average flow characteristics of the tip wake. The time-domain response of the time coefficients remains an approximate constant of the vorticity and velocity modulus fields, and the curve of the static pressure field fluctuates complexly. The 2ndand 3rd-order flow modes of the physical fields should be the energy mapping of the tip spiral wake, where the impeller surface has a remarkable circumferential symmetry. For the subsequent high-order flow modes, there are differences in the co-order modes of different physical parameter fields due to the influence of attached vortices detached from the blade surface and the X-axial velocity wake. As the order increases, the variation of the spatial modes has three stages, except for the 1st-mode. The first stage is that the order flow modes projected by the blade tip wake has significant encrypted circumferential symmetry and spiral characteristics. The second stage is that the order flow modes projected by the attached vortex and X-axial velocity fluctuate more randomly. The third stage is that the order flow modes projected by the deep fusion of the tip wake and attached vortex or X-axial velocity wake has further refined circumferential symmetry and random fluctuation characteristics. As the mode order increases, the number of local flow structure distributed symmetrically along the circumference increases by a multiple of 3, which is the physical number of impeller blades in the projection mode dominated by the energy of the blade tip wake. This also corresponds to the time-domain equivalent dual-frequency variation characteristics of the modal time coefficient and the frequency-domain dual-frequency characteristics. There are a series of time-frequency variations, which have been discussed in detail for the time coefficients of different mode stages. The fusion phase at this depth reflects the quasi-resonance mechanism of the local wake flow structure of the blade tip vortices. At the same time, the rotating wake field has distinct characteristics in the energetic dominance, especially in the velocity modulus field. The proposed method and procedure for solving the multi-level solution of the wake of the rotational flow have the potential to be applied in other complex fields of fluid mechanics.

FUNDING

This research was funded by the Chongqing Natural Science Foundation of China (No.cstc2020jcyj-msxmX0314), the Ningxia Key Research and Development Program of Foreign Science and Technology Cooperation Projects(No.202204), the National Science and Technology Major Project (No.J2022-IV-0010-0024), the Key Scientific Research Project in the Higher Education Institutions from the Ningxia Education Department(No.2022115), and the PhD Start-up Fund from Chongqing University of Science and Technology (No.181903017).

ACKNOWLEDGMENTS

We sincerely acknowledge the key laboratory of wind and solar power energy utilization technology ministry of education in China (Inner Mongolia University of Technology) for providing the relevant experimental data.

REFERENCES

[1] Singh, A. K., Jyoti, B., Kumar, S., & Lenka, S. K., "Assessment of Global Sustainable Development, Environmental Sustainability, Economic Development and Social Development Index in Selected Economies", International Journal of Sustainable Development and Planning, 2021, 16(1): p. 123-138. DOI:10.18280/ijsdp.160113

[2] Sanderse, B., Van der Pijl, S. P., & Koren, B., "Review of Computational Fluid Dynamics for Wind Turbine Wake Aerodynamics", Wind energy, 2011, 14(7): p. 799-819. DOI:10.1002/we.458

[3] Bouhelal, A., Smaili, A., Guerri, O., & Masson, C., "Numerical Investigations on the Fluid Behavior in the Near Wake of an Experimental Wind Turbine Model in the Presence of the Nacelle", Journal of Applied Fluid Mechanics, 2022, 16(1): p. 21-33. DOI:10.47176/jafm.16.01.1382

[4] He, X., Geng, H., Mu, G., "Modeling of Wind Turbine Generators for Power System Stability Studies: A Review", Renewable and Sustainable Energy Reviews, 2021, 143(1): p. 110865. DOI:10.1016/j.rser.2021.110865

[5] Maeda, T., Kamada, Y., Murata, J., Yonekura, S., Ito, T., Okawa, A., & Kogaki, T., "Wind Tunnel Study on Wind and Turbulence Intensity Profiles in Wind Turbine Wake", Journal of Thermal Science, 2011, 20(2): p. 127-132. DOI: 10.1007/s11630-011-0446-9

[6] Talavera, M., & Shu, F., "Experimental Study of Turbulence Intensity Influence on Wind Turbine Performance and Wake Recovery in a Low-speed Wind Tunnel", Renewable Energy, 2017, 109(1): p. 363-371. DOI:10.1016/j.renene.2017.03.034

[7] Han, Y., Wang, J., Sun, B., Dong, X., Li, X., "Experimental Study on Influence Mechanism of Turbulent Intensity on Velocity Recovery of Horizontal Axis Wind Turbine Wake (In Chinese)", Acta Energiae Solaris Sinica, 2019, 40(3): p. 649-655. DOI: 10.19912/j.0254-0096.2019.03.008

[8] Vahidi, D., & Porté-Agel, F., "A Physics-based Model for Wind Turbine Wake Expansion in the Atmospheric Boundary Layer", Journal of Fluid Mechanics, 2022, 943(1): p. A49. DOI:10.1017/jfm.2022.443

[9] Gui, X., Xue, H., Su, S., Hu, Z., & Xu, Y., "Study on Aerodynamic Performance of Mine Air Duct Horizontal Axis Wind Turbine based on Breeze Power Generation", Energy Science & Engineering, 2022, 10(4): p. 1132-1152. DOI:10.1002/ese3.1081

[10] Hassanpour, M., Azadani, L. N., "Aerodynamic Optimization of the Configuration of a Pair of Vertical Axis Wind Turbines", Energy Conversion and Management, 2021, 238: p. 114069. DOI:10.1016/j.enconman.2021.114069

[11] Koca, K., Genç, M. S., Bayır, E., Soğuksu, F., "Experimental Study of the Wind Turbine Airfoil with the Local Flexibility at Different Locations for More Energy Output", Energy, 2022, 239(Part A): p. 121887. DOI:10.1016/j.energy.2021.121887

[12] Su, R., Gao, Z., Chen, Y., Zhang, C., Wang, J., "Large-eddy Simulation of the Influence of Hairpin Vortex on Pressure Coefficient of an Operating Horizontal Axis Wind Turbine", Energy Conversion and Management, 2022, 267: p. 115864. DOI:10.1016/j.enconman.2022.115864

[13] Xu, B., Feng, J., Wang, T., Yuan, Y., Zhao, Z., "Application of a Turbulent Vortex Core Model in the Free Vortex Wake Scheme to Predict Wind Turbine Aerodynamics", Journal of Renewable and Sustainable Energy, 2018, 10(2): p. 023303. DOI:10.1063/1.5020200

[14] Xu, B., Liu, B., Feng, J., Lu, Z., "Influence of Vortex Core Size on Aerodynamic Calculation of Wind Turbine in Free Vortex Wake Method", Chinese Journal of Theoretical and Applied Mechanics, 2019, 51(5): p. 1530-1537. DOI:10.6052/0459-1879-18-440

[15] Marten, D., Paschereit, C. O., Huang, X., Meinke, M., Schröder, W., Müller, J., "Oberleithner, K. Predicting Wind Turbine Wake Breakdown Using a Free Vortex Wake Code", AIAA Journal, 2020, 58(11): p. 4672-4685. DOI:10.2514/1.J058308

[16] Rezaeiha, A., Montazeri, H., Blocken B., "CFD Analysis of Dynamic Stall on Vertical Axis Wind Turbines Using Scale-Adaptive Simulation (SAS): Comparison against URANS and Hybrid RANS/LES", Energy Conversion and Management, 2019, 196: p. 1282-1298. DOI:10.1016/j.enconman.2019.06.081

[17] De Cillis, G., Cherubini, S., Semeraro, O., Leonardi, S., & De Palma, P., "POD-based analysis of a wind turbine wake under the influence of tower and nacelle", Wind Energy, 2021, 24(6): p. 609-633. https://doi.org/10.1002/we.2592

[18] De Cillis, G., Cherubini, S., Semeraro, O., Leonardi, S., & De Palma, P., "Stability and optimal forcing analysis of a wind turbine wake: Comparison with POD", Renewable Energy, 2022, 181: p. 765-785. https://doi.org/10.1016/j.renene.2021.09.025

[19] Hamilton, N., Viggiano, B., Calaf, M., Tutkun, M., & Cal, R. B., "A generalized framework for reduced-order modeling of a wind turbine wake", Wind Energy, 2018, 21(6): p. 373-390,. https://doi.org/10.1002/we.2167

[20] Wood, D. H., & Hammam, M. M., "Optimal performance of actuator disc models for horizontal-axis turbines", Frontiers in Energy Research, 2022, 10: p. 971177. https://doi.org/10.3389/fenrg.2022.971177

[21] Versteeg, H. K., and Malalasekera, W., An Introduction to computational fluid dynamics: The finite volume method, second edition, 2007.

[22] Kutz, J N., "Deep Learning in Fluid Dynamics", Journal of Fluid Mechanics, 2017, 814: p. 1-4. DOI:10.1017/jfm.2016.803

[23] Ling, J., Kurzawski, A., Templeton, J., "Reynolds Averaged Turbulence Modelling Using Deep Neural Networks with Embedded Invariance", Journal of Fluid Mechanics, 2016, 807: p. 155-166. DOI:10.1017/jfm.2016.615

[24] Sirovich, L., "Turbulence and the Dynamics of Coherent Structures. I. Coherent Structures", Quarterly of applied mathematics, 1987, 45(3): p. 561-571. DOI:10.1090/qam/910462

[25] Sirovich, L., "Turbulence and the dynamics of coherent structures. I-Coherent structures. II-Symmetries and transformations", III-Dynamics and scaling. Quarterly of Applied Mathematics, 1987, 45(3): p. 561-571.

[26] Lucia, D. J., Beran, P. S., Silva, W. A., "Reduced-order Modeling: New Approaches for Computational Physics", Progress in Aerospace Sciences, 2004, 40(1-2): p. 51-117. DOI:10.1016/j.paerosci.2003.12.001

[27] Rahman, A., Redwan, D. A., Thohura, S., Kamrujjaman, M., Molla, M. M., "Natural Convection and Entropy Generation of Non-Newtonian Nanofluids with Different Angles of External Magnetic Field using GPU Accelerated MRT-LBM", Case Studies in Thermal Engineering, 2022, 30: p. 101769. DOI:10.1016/j.csite.2022.101769

[28] Bai, J., Hu, X., Tao, Y. H., Ji, W., "Investigation of Non-Newtonian Power-law Free Convection Affected by a Magnetic Field in an Inclined Quarter-circle Chamber Containing the Lozenge-shaped Obstacle via MRT-LBM of First and Second laws of Thermodynamics", Engineering Analysis with Boundary Elements, 2022, 145: p. 335-351. DOI:10.1016/j.enganabound.2022.09.022

[29] Chávez-Modena, M., Ferrer, E., Rubio, G., "Improving the Stability of Multiple-relaxation Lattice Boltzmann Methods with Central Moments", Computers & Fluids, 2018, 172: p. 397-409. DOI:10.1016/j.compfluid.2018.03.084

[30] Buffa, E., Jacob, J., Sagaut, P., "Lattice-Boltzmann-based Large-eddy Simulation of High-rise Building Aerodynamics with Inlet Turbulence Reconstruction", Journal of Wind Engineering and Industrial Aerodynamics, 2021, 212: p. 104560. DOI:10.1016/j.jweia.2021.104560

[31] Dai, S., Tang, D., Younis, B. A., "Extended Wall-adapting Local Eddy-viscosity Model for the Large-eddy Simulations of Multiscale Flows", Physics of Fluids, 2022, 34(5): p. 055117. DOI:10.1063/5.0088656